DELFT UNIVERSITY OF TECHNOLOGY

MASTER THESIS

Testing DNS capability of OpenFOAM and STAR-CCM+

In support of thermal fatigue assessment for complex geometries

Author:
S.W. VAN HAREN
student number: 1184261

Tutors:
TU Delft:
Dr. ir. Marc Gerritsma
NRG:
ir. Ed Komen

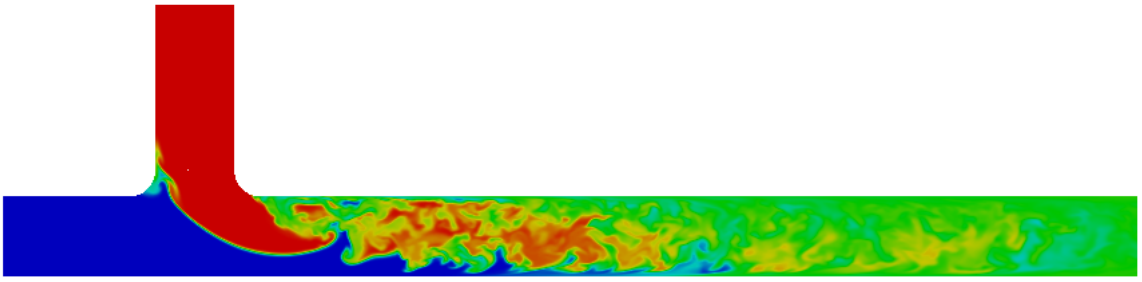

Mixing of a hot (red) and cold (blue) fluid in a T-junction geometry. Flow is from left to right in the horizontal pipe, and from top to bottom in the vertical pipe.

May 31, 2011

Contents

List of symbols

Greek Symbols

α . . . . . thermal diffusivity
β . . . . . thermal expansion coefficient
Γ_ϕ . . . . . diffusion coefficient of ϕ
δ . . . . . channel half height/pipe radius
δ_{ij} . . . . . Kronecker delta
ϵ . . . . . dissipation rate of the turbulent kinetic energy
η . . . . . Kolmogorov length scale
η_θ . . . . . Batchelor length scale
ν . . . . . kinematic viscosity
ρ . . . . . density
τ . . . . . Kolmogorov time scale
τ_w . . . . . wall friction
ϕ . . . . . transported scalar, turbulent quantity

English Symbols

a . . . . . general vector property
b . . . . . thermal effusivity
c_p . . . . . specific heat at constant pressure
d . . . . . wall thickness
d . . . . . vector connecting cell centers N and P
k . . . . . thermal conductivity
K . . . . . activity ratio
L . . . . . length scale
L_x . . . . . length of channel/pipe
L_z . . . . . width of channel
m . . . . . mass in channel/pipe
n . . . . . wall-normal coordinate
p . . . . . pressure
$\tilde{p}$ . . . . . periodic pressure
q_w . . . . . wall-to-fluid heat flux
R . . . . . pipe radius
S . . . . . face area vector
t . . . . . time coordinate
T . . . . . temperature
$\tilde{T}$ . . . . . periodic temperature
T_τ . . . . . friction temperature
u_τ . . . . . friction velocity
u, v, w . . . . . x,y,z component of velocity vector

U . . . . . velocity scale
U . . . . . velocity vector
v . . . . . Kolmogorov velocity scale
x . . . . . position vector

Subscripts

$bulk$ . . . . . bulk average (volume average over entire domain)
f . . . . . fluid
N . . . . . cell center neighbour cell
P . . . . . cell center current cell
rms . . . . . root mean squared
s . . . . . solid
w . . . . . wall

Superscripts

$+$ . . . . . normalized by viscous scales
$++$ . . . . . normalized by viscous scales
$n, n-1, n-2$ . . . . . timestep (current, previous, second previous)

Abbreviations

CDS . . . . . convection differencing scheme
CFD . . . . . computational fluid dynamics
CFL . . . . . Courant-Friedrichs-Lewy condition
DNS . . . . . direct numerical simulation
DES . . . . . detached eddy simulation
FDM . . . . . finite difference method
FVM . . . . . finite volume method
LES . . . . . large eddy simulation
PISO . . . . . pressure-implicit with splitting of operators
PWR . . . . . pressurized water reactor
RANS . . . . . Reynolds-averaged Navier-Stokes equations
RMS . . . . . root-mean-squared
SIMPLE . . . . . semi-implicit method for pressure-linked equations
SR . . . . . stretching ratio
URANS . . . . . Unsteady Reynolds-averaged Navier-Stokes equations

Acknowledgements

Making this thesis would certainly not have been possible without the help and enthousiasm of a lot of people. Therefore, it seems right to start this thesis by acknowledging their work.

First of all, I would like to thank all my colleagues at the Nuclear Research and Consultancy Group in Petten, as well as the other interns there. The door was always open for my questions. Out of these colleagues, I would mostly like to thank Ed Komen for his guidance. Also, thanks go out to Marc Gerritsma for his role as my tutor.

A lot of people helped me during my thesis by taking the time for questions and discussions. In random order, I would like to thank Arthur Veldman, Wim-Paul Breugem, Bojan Niceno, Iztok Tiselj and Laurent Bricteux for this.

Also many thanks must go out to Faibio Canesin and Florian Krause, for supplying me with their own code written for OpenFOAM.

Special thanks to my family and all my friends for sticking up with me.

Last but not least, thank you Dennis Ernens and Melanie Stuiver for being my 'Study Buddies'. You made all the work leading up to this thesis a lot of fun.

1. Introduction

Let us start this thesis using a famous quote from Bertrand Russell:

> The whole problem with the world is that fools and fanatics are always so certain of themselves, but wiser people so full of doubts

This quote denotes the spirit of this thesis. As I have tried to be wiser than a fool, I tried to keep doubt constantly present in my mind. At first I tried to remove my doubts by rigorously comparing my results with references. And when there were no more references available to guide me, I had to resort to doubt itself to analyze the results.

This introduction will start by discussing the problem of thermal fatigue in section 1.1. Based on this problem some objectives for this thesis are formulated in section 1.2. How these objectives were achieved is presented in section 1.3. An outline of this thesis is given in section 1.4.

1.1. The problem of thermal fatigue

All the work performed in this thesis serves to help understand failure of structural parts due to thermal fatigue. So what is thermal fatigue? First, fatigue will be explained and second, thermal fatigue is explained. Fatigue is well known amongst engineers as the failure of a structural part due to cyclic stresses, when these stresses are below the ultimate stress (the stress at which the part will fail) for a static load. In general these stresses will be imposed by external loading, for instance due to aerodynamic loading of a wing. Thermal fatigue is a special type of fatigue, for this case the cyclic stresses are imposed by thermal stresses. So what are thermal stresses? A structural part will in general expand or contract due to a variation in its temperature. If this expansion or contraction is restraint, stresses will occur. The restraint can be imposed by external clamping of the structural part, or by different magnitudes of expansion in different places within the structural part. Different magnitudes of expansion within a structural part can be caused by local temperature variations. If these temperature variations are present both in space (giving thermal stresses) and in time (giving cyclic thermal stresses) thermal fatigue can occur provided that the amplitude of the temperature variation is large enough [5].

Thermal fatigue is an important issue in the operation of nuclear power plants. Especially the nuclear power plants of the type pressurized water reactor (PWR) are susceptible to thermal fatigue. The temperature of the structural parts, such as pipes, is

strongly inlfuenced by the coolant (water for a PWR) flowing through it. All the mechanisms describes above for thermal fatigue are present in these pipes. Due to different coolant temperatures in different pipes, temperature variations in space are present. In places where hot and cold streams mix (such as in a T-junctions, this can be seen on the cover) temperature varies strongly over small distances. Since this mixing process is turbulent, and therefore unsteady, the temperature field will also vary in time in these mixing zones. The amplitude of these variations is large due to the large amount of heat transported away from the nuclear core ,and due to the fact that the water is pressurized. Temperature differences between hot and cold streams can be up to 160° Celsius [31].

A well known failure, due to thermal fatigue, of a T-junction occured in the Civaux nuclear power plant in 1998 [27], after only 1500 hours of operation. Other incidents occured in the Japanese Tsuruga-2 PWR in 1999 and the Japanese Tomari-2 PWR in 2003 [19].

To avoid these failures, the mechanisms of thermal fatigue must be understood. This thesis will focus on the mixing of hot and cold streams of coolant, this mixing imposes the thermal stresses on the structural material. This leads to the wish to understand the temperature fluctuations in the mixing zones. If the mixing could be properly simulated (or measured in experiments) detailed analysis could be performed on the spatial variations of temperature, giving information on the locations and amplitudes of the thermal stresses. Knowledge about the variation of the temperature field in time will give information about the frequency of the thermal stresses.

To further understand the mixing between the hot and cold streams of coolant, and to investigate the temperature fluctuations at the wall, quite some research has been done. Both experimentally and using computational fluid dynamics (CFD). Since especially the correct prediction of the fluctuations in the temperature are of importance, the numerical methods used is often a large eddy simulation (LES) [7, 19, 22, 23, 35]. The extension of the Reynolds averaged Navier-Stokes equations (RANS) to the Unsteady RANS (URANS) has also been tested for the T-junction [24]. To my knowledge only one direct numerical simulation (DNS) is available in literature [15]. However, the approach taken for the DNS performed by Fukushima [15] is different from the approach adopted in this thesis. Fukushima changed the geometry of the T-junction to accomodate the structured numerical method (instead of circular pipes square channels were used to create the geometry). Experiments are also available [15, 35].

However, when reading these references it can be seen that accurate near-wall data is not available. Simulations available in literature often use wall-functions for which it is known that accurate prediction of the near-wall flow is not possible. Therefore, accurate prediction of the heat-flux from the fluid to the wall is not possible [8, 19]. In the experiments accurate near-wall data is also not available, since measuring equipment fails to measure close to the wall. Knowing the limitations in current CFD-codes it is not possible to use CFD as a straightforward design tool concerning thermal fatigue at this moment. It is also not possible to understand the general dynamics of heat transfer. A general picture of the flow dynamics can be given by cheaper methods than DNS (such as RANS, LES or URANS), but the finer details of the flow can not be predicted by these methods.

So, is there any hope for the future to accurately understand the mixing of hot and cold fluid, and how it imposes thermal stresses? Using a DNS one could certainly accurately calculate the mixing of the streams and the heat transfer at the wall. However, the cost of performing a DNS at industrial Reynolds numbers is too high. Other methods could be promising, such as a detached eddy simulation (DES) in which one would accurately calculate the boundary layer and would use a relative cheap method to calculate the bulk flow. A wall-resolved LES could also be a possibility, a drawback of the wall-resolved LES is the fact that the cost of the simulation approaches the cost for a DNS.

Futhermore, it is know that using one of the standard boundary conditions at a wall for the temperature equation (the isothermal or adiabatic wall) is not accurate in predicting the heat flux between the solid and the fluid [33]. In general a wall will not have a constant temperature, violating the isothermal boundary condition, and heat will flow from the fluid to the wall or vice versa, violating the adiabatic wall boundary condition [33]. Therefore this thesis also explores the possibilties of conjugate heat transfer. A conjugate heat transfer simulation is a simulation where the heat transport is also solved for in the wall.

This thesis will work towards performing a DNS in a T-junction geometry. Off course this DNS will have to be performed at low Reynolds number. However the goal of such a simulation is twofold. First of all, the finer details of the mixing process can be investigated and understood. However, care must taken to extend this understanding at small Reynolds numbers to industrial Reynolds numbers. Secondly, such a DNS can be used to validate cheaper methods.

Summarizing, the wish was put forward to perform a DNS of a T-junction geometry. This calls for the use of CFD methods applicable in such a geometry. At first, it must be assessed if these methods can be used at all to perform a DNS. This is the main goal of this thesis.

1.2. Objective of this thesis

The objective of this thesis can be summarized as follows:

- Assess DNS accurracy of OpenFOAM and STAR-CCM+ for channel and pipe flows
- Assess DNS accurracy of OpenFOAM and STAR-CCM+ using complex cell types, which are needed for meshing of complex geometries
- Perform demonstration of a DNS in a complex geometry (T-junction)

1.3. Motivation of selected approach

To asses the accuracy of the OpenFOAM [26] and STAR-CCM+ [6] solvers first the simplest direct numerical simulations were performed, the channel flows. The channel flow was simulated including heat transfer, both for non-conjugate and conjugate heat transfer. After this, the turbulent pipe flow was simulated. This is already a bit more challenging for the solvers, since the pipe needs to be meshed using more complex cell types than the channel. Two slightly different cell types were used to mesh the pipe. Both these cell types are needed to mesh the T-junction geometry. Finally, all that was learned during the channel and pipe flow simulations was put into practice for the T-junction simulation.

1.4. Thesis outline

The outline for the thesis will be as follows:

Chapter 2	Introduction to some turbulence theory important for this thesis
Chapter 3	Description of the numerical method used
Chapter 4	Results for the channel and pipe flow simulations
Chapter 5	Results for the demonstration DNS in a T-junction
Chapter 6	Discussion of results, recommendations and conclusions
Chapter 7	Summary of this thesis

2. Turbulence

This chapter is not intended to be a complete introduction to turbulence theory. This chapter merely highlights aspects of turbulence important for a DNS. Section 2.1 discusses some general features of turbulent flows important for a direct numerical simulation. In section 2.2 the different scales in turbulent flows are described. These scales are often used to non-dimensionalize the results, this is described in section 2.3. Since wall-bounded turbulent flow is considered in this thesis some of the special aspects of wall-bounded turbulence is discussed in section 2.4.

2.1. Introduction to turbulence

In this thesis a turbulent flow will be simulated. So it is important to take a minute and discuss what a turbulent flow is. Furthermore, all flows simulated in this thesis are a special type of turbulent flow. All the flows are assumed to be statistically steady, or fully developed. This yields the ability to split any quantity ϕ (such as velocity, temperature or pressure) in a mean and fluctuating component:

$$\phi(\mathbf{x}, t) = \overline{\phi}(\mathbf{x}) + \phi^{'}(\mathbf{x}, t) \tag{2.1.1}$$

In this splitting the instantaneous field $\phi(\mathbf{x}, t)$ is split in a mean component $\overline{\phi}(\mathbf{x})$ and a fluctuating component $\phi^{'}(\mathbf{x}, t)$, see figure 2.1. As can be seen the mean $\overline{\phi}(\mathbf{x})$ is given as a function of the position vector $\mathbf{x}$, this means averaging is only performed over time. For some flows it is possible to make use of the symmetry or periodicity of the flow, and averaging can also be performed over spatial coordinates. In this case the mean will in general be a function of less coordinates (for instance only a function of y).

It is important to check if the quantity ϕ can be assumed to be statistically steady. Especially in the beginning of a simulation the flow will in general not be fully developed, this is illustrated in figure 2.2.

It is common practice to compared the root-mean-square (RMS) of the fluctuations between different simulations. The root-mean-square of the fluctuation is calculated as [28]:

$$\phi_{rms}(\mathbf{x}) = \sqrt{\overline{(\phi^{'}(\mathbf{x}, t))^2}} \tag{2.1.2}$$

Again, the RMS can be a function of less spatial coordinates if the geometry permits.

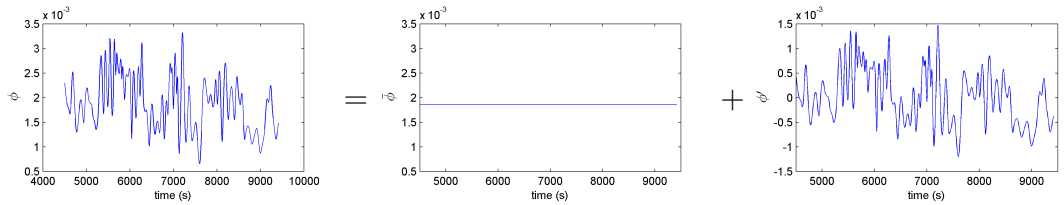

Figure 2.1.: The splitting of an instantaneous field ϕ into a mean component $\overline{\phi}$ and a fluctuating component ϕ'.

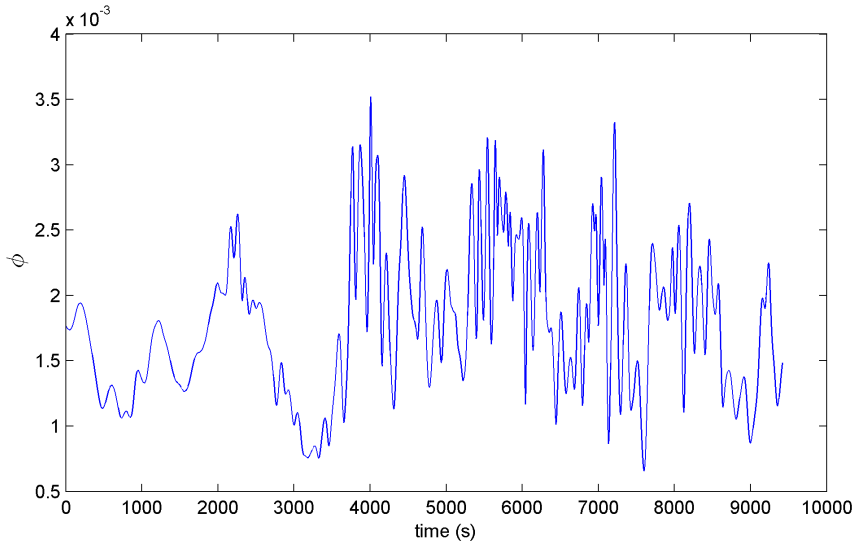

Figure 2.2.: Development of a turbulent signal. The high frequency components in the fully developed part of the signal are not present in the first few thousand seconds of the signal.

Turbulent flows are characterized by non-dimensional parameters, which are encountered often in literature. This section lists a few non-dimensional parameters which are important for turbulent flows.

The first and most important non-dimensional parameters influencing the properties of a turbulent flow is the Reynolds number, based on a velocity scale U, length scale L and the kinematic viscosity ν:

$$Re = \frac{UL}{\nu} \tag{2.1.3}$$

The Reynolds number determines the ratio between inertial forces and viscous forces. For a low Reynolds number the viscous forces are dominant, and for a high Reynolds number the inertial forces are dominant.

The second important non-dimensional number is the Prandtl number, the ratio between the kinematic viscosity ν and the thermal diffusivity α.:

$$Pr = \frac{\nu}{\alpha} \tag{2.1.4}$$

For high Prandtl numbers the thermal diffusion is weak compared to the momentum diffusion, and for low Prandtl numbers the thermal diffusion is strong compared to the momentum diffusion.

For the third important non-dimensional number, the activity ratio, the thermal effusivity needs to be defined first [8], based on the density ρ, specific heat c_p and thermal conductivity k:

$$b = \sqrt{\rho c_p k} \tag{2.1.5}$$

The thermal effusivity determines the response of a medium to a sudden change in temperature at the boundary [8].

The activity ratio is the ratio of the thermal effusivity of the fluid and the thermal effusivity of the solid [8, 33]:

$$K = \frac{b_f}{b_s} \tag{2.1.6}$$

To understand the influence of the activity ratio on the thermal field in a fluid, it must be realized that the activity ratio is also set for heat transfer problems which are solved without conjugate heat transfer. An adiabatic wall corresponds to an activity ratio of $K = \infty$, and a wall at fixed temperature corresponds to an activity ratio of $K = 0$. These boundary conditions are limit cases. In reality a fluid/solid system will have an activity ratio somewhere between ∞ and 0. Next to the activity ratio, the behaviour of a fluid/solid system is also influenced by the (non-dimensional) wall-thickness, see Section 2.3. In experiments it has been shown that the isothermal boundary condition can be realized with a solid/fluid system of a thick copper wall and water, and isoflux conditions can be achieved with a solid/fluid system of water and a very thin solid wall [33].

2.2. Turbulent scales

Turbulence is characterized by a large range in scales. A turbulent flow will contain different length scales, velocity scales and temporal scales. In a typical turbulent signal, such as in figure 2.2, these different scales can be recognized as different frequencies.

The largest scales in a flow are characterized by a length scale L, based on a geometric parameter, a velocity scale U, which could be the mean velocity for instance, and a time

scale defined by L/U [11]. The Reynolds number is defined as a function of these large scales (see Equation 2.1.3). The large scales are also named large eddies.

Kinetic energy is transferred from the large scales to the smaller scales along the energy cascade. In the energy cascade, energy is transferred from the large eddies to smaller eddies until the eddies are so small that viscous effects dominate and kinetic energy is transformed into heat. The energy cascade is visualized in Figure 2.3. Dimensional analysis performed by Kolmogorov provides us with expressions for these smallest scales, or eddies. The length scale η, velocity scale v and time scale τ are expressed by [20]:

$$\eta = \left(\frac{\nu^3}{\epsilon}\right)^{\frac{1}{4}} \quad v = (\nu\epsilon)^{\frac{1}{4}} \quad \tau = \left(\frac{\nu}{\epsilon}\right)^{\frac{1}{2}} \tag{2.2.1}$$

$$\frac{\eta}{L} \sim Re^{-\frac{3}{4}} \quad \frac{v}{U} \sim Re^{-\frac{1}{4}} \quad \frac{\tau}{L/U} \sim Re^{-\frac{1}{2}} \tag{2.2.2}$$

If heat transfer is simulated, scales also exist for the temperature, the smallest temperature length scales are named the Batchelor length scale and are also derived using dimensional analysis [2, 9]:

$$\eta_\theta = \left(\frac{\alpha^2\nu}{\epsilon}\right)^{\frac{1}{4}} \quad \text{for} \quad \alpha < \nu \tag{2.2.3}$$

$$\eta_\theta = \left(\frac{\alpha^3}{\epsilon}\right)^{\frac{1}{4}} \quad \text{for} \quad \alpha \geq \nu \tag{2.2.4}$$

In these definitions ϵ is the dissipation rate of the turbulent kinetic energy [21, 28]:

$$\epsilon = \nu\overline{\left(\frac{\partial u_i'}{\partial x_k}\right)^2} \tag{2.2.5}$$

The double definition of the Batchelor scale stems from the different physical behaviour of the two different possible cases of the Batchelor scale being larger or smaller than the Kolmogorov scale [2, 9].

The ratio of the Kolmogorov and Batchelor scales can be conveniently expressed using the Prandtl number:

$$\frac{\eta_\theta}{\eta} = Pr^{-1/2} \quad \text{for} \quad \alpha < \nu \tag{2.2.6}$$

$$\frac{\eta_\theta}{\eta} = Pr^{-3/4} \quad \text{for} \quad \alpha \geq \nu \tag{2.2.7}$$

The Kolmogorov and Batchelor scale are important for a direct numerical simulation, since a direct numerical simulation attempts to capture all the scales of the flow. It was shown in this section that the Kolmogorov scale will decrease for increasing Reynolds number and the Batchelor length scale will decrease for increasing Prandtl number. Thus increasing the Reynolds number or the Prandtl number yields the need for mesh refinement.

2.3. Scaling of results

It is customary and convenient to non-dimensionalize (or scale) the variables in a turbulent flow. The velocity used for scaling is often the friction velocity u_τ, the temperatures used for scaling are often the friction temperature T_τ and the wall temperature T_w. Furthermore, physical constants are used for scaling (ν and α) and length scales (L).

The friction velocity is calculated from the wall friction using the viscous shear stress, since the turbulent stress is zero at the wall [28].

$$u_\tau = \sqrt{\frac{\tau_w}{\rho}} = \sqrt{\nu \left(\frac{\partial \overline{u}}{\partial n}\right)_w} \tag{2.3.1}$$

Please note that this is a rather simplified formula derived from the axial mean momentum equation [28]. This equation is therefore only valid if flows are one-dimensional in the mean (such as pipe and channel flows). A more general way of deriving the shear stress at a wall is to multiply the stress tensor with the surface normal vector yielding the local stress vector. This vector can be split in a normal and tangential component.

The friction temperature is given by [8]:

$$T_\tau = \frac{\alpha_f}{u_\tau} \left(\frac{\partial T}{\partial n}\right)_w = \frac{q_w}{u_\tau \rho c_p} \tag{2.3.2}$$

The scaling of spatial coordinates in a fluid, and the scaling of velocities are well-known:

$$L^+ = \frac{u_\tau L}{\nu} \tag{2.3.3}$$

$$U^+ = \frac{U}{u_\tau} \tag{2.3.4}$$

Lengths non-dimensionalized as above are expressed in so-called wall-units.

The scaling for the temperature is performed as follows:

$$T^+ = \frac{T - T_w}{T_\tau} \tag{2.3.5}$$

The scaling used for spatial coordinates in a solid is less well known [8][33]:

$$L^{++} = L\frac{u_\tau}{\nu}\sqrt{\frac{\alpha_f}{\alpha s}} \tag{2.3.6}$$

This scaling might look strange but it appears naturally if one non-dimensionalizes the temperature equation (3.1.4) in a solid [8].

Time is scaled using:

$$t^+ = t\frac{u_\tau}{L} \tag{2.3.7}$$

The scaling given above is used throughout this thesis. However, a second definition is sometimes used in literature:

$$t^+ = t\frac{u_\tau^2}{\nu} \tag{2.3.8}$$

This second definition is given here, since the term non-dimensional time can be confusing when reading literature.

2.4. Wall-bounded turbulent flows

To understand wall-bounded turbulent flows one must take a step back in complexity towards isotropic tubulent flows. Isotropic turbulent flows will be described first in this section. Next, relatively simple wall-bounded flows will be discussed such as channel or pipe flows. Last but not least this will be extended to flows in complex geometries, such as T-junctions.

The simplest turbulent flow imaginable is the isotropic box of turbulence. In the isotropic box large scales will transfer their energy to smaller scales until the scales are so small that the energy is destroyed by diffusion. This is the well-known energy cascade (see Figure 2.3).

A slightly more complex turbulent flow is the flow through a straight channel (or pipe). Next to the energy cascade other flow dynamics will be present. The wall-friction will

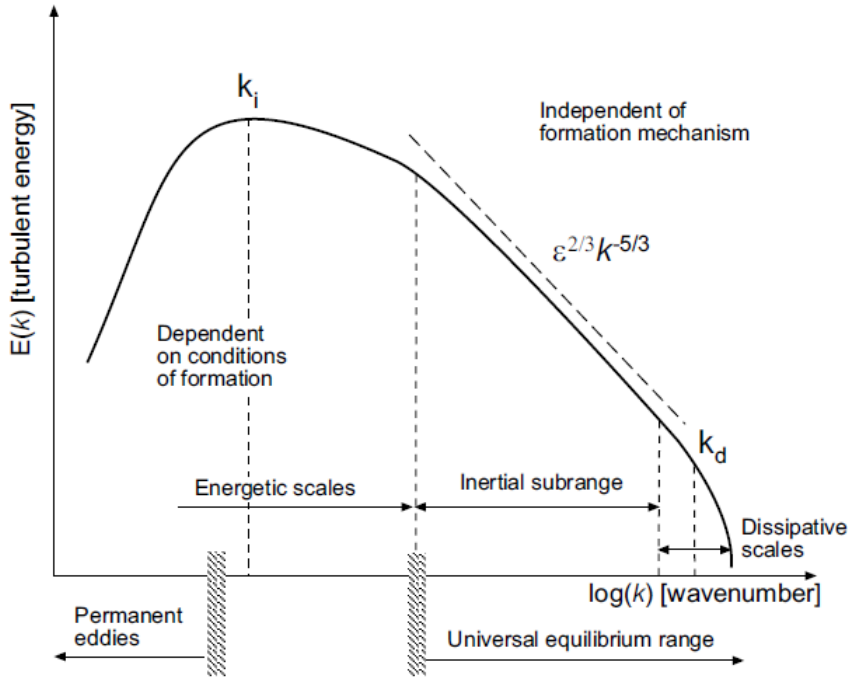

Figure 2.3.: The energy cascade. At small wavenumbers energy is fed into the flow. The energy is fed to smaller eddies in the inertial subrange until eddies are so small that viscosity dissipates the energy. [10]

generate a shear layer. For simple wall-bounded flows such as in channels and pipes a well-known mean velocity profiles will be present, known as the law of the wall (see Figure 2.4). However, it must be realized that this profile will only be present in cases which are characterized by a gently favorable pressure gradient.

First consider the case of sliglty favorable pressure gradient. The mean profile will consist of the inner layer, outer layer and overlap layer. In the inner layer the mean velocity profile is linear and extends to about $y^+ = 5$. The overlap layer consists of a logarithmic profile. The size of the overlap layer is strongly dependent on the pressure gradient. It can be very thick for favorable gradients (a few thousand y^+), it can be thin for adverse pressure gradients (a few hunderd y^+) or it can be non-existent for strongly adverse pressure gradient when the flow seperates [36].

Turbulence is chaotic by definition but a lot of work has also been done in identifying coherent structures in the chaos [28]. This section discusses some coherent structures observed in boundary layers. For flows driven by gentle favorable pressure gradients, such as channel and pipe flows, which are allowed to fully develop, coherent structures in the boundary layer can be recognized. The low and high speed streaks are well known and associated with the peak in u_{rms} as can be seen in for instance figure 4.3. At the interface between the low and high speed streaks vortices are formed. These vortices will lift the low-speed streaks out of the buffer layer into the logarithmic layer. This process of streaks, vortex forming and the consequent lifting of streaks is called the streak-instability cycle. This cycle is self-sustaining. For this reason turbulent pipe and channel flows will remain turbulent once turbulent, as long as the Reynolds number is

large enough. If the Reynolds number is too small the diffusion at the interface between the low and high speed streaks will be able to dampen the streak-instability cycle [10].

But why are these coherent structures of interest to us in the context of thermal fatigue? These structures are interesting since the turbulent structures in the boundary layer existing close to the wall are visible in the temperature fields of the wall. These structures on the wall are known as thermal streaks and are visualized in figure 4.13.

Moving to more complex wall-bounded flows (such as a T-junction) even more complex flow dynamics will be present. Next to the energy cascade and the shear layer generated by the wall-friction, complex dynamics such as seperation and mixing layers will be present.

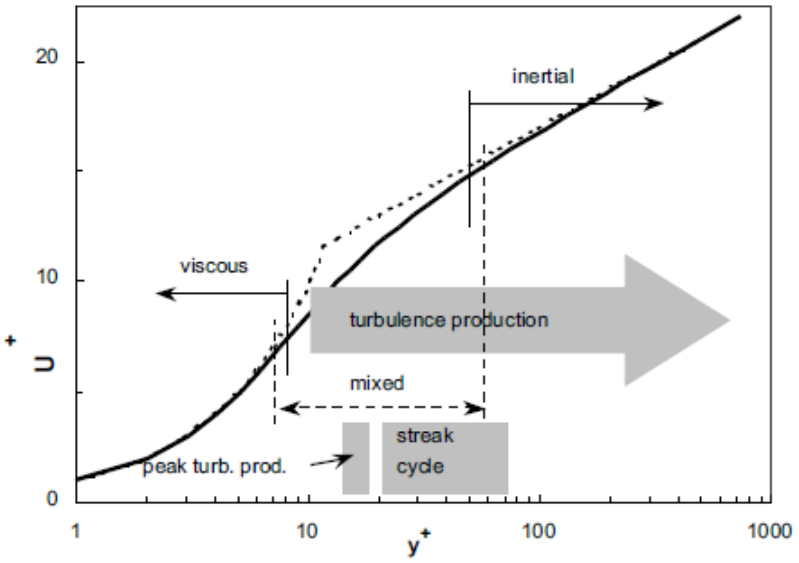

Figure 2.4.: Velocity profile for a fully developed wall-bounded flow. [10]

3. Numerical method

The numerical method used is at the beating heart of a direct numerical simulation, this is in contrast with a RANS simulation or a LES, where the model also greatly influences the results. The order of accuracy of the numerical method should be high and the influence on the dissipation at the small scales should be minimal. Therefore it is important that numerical errors are kept to a minimum. However, the method should also be applicable in complex geometries. This makes the need of numerical methods usable on unstructered grids highly desirable. Other solutions to tackle this problem exist, a discussion will be devoted to this in Section 6.

In section 3.1 the governing equations used in this thesis are presented. Section 3.2 discusses how the system of equations is solved in OpenFOAM and STAR-CCM+, and how the non-linearity of the momentum equation is treated in OpenFOAM. Section 3.4 discusses some drawbacks of the numerical method which is used. For a full treatment of the discretization used in OpenFOAM please read appendix A.

3.1. Governing equations

Throughout this thesis the following equations are solved: The incompressible Navier-Stokes equations [1, 36]. It is important to keep in mind the assumptions which were used during the derivation:

- incompressible flow ($\rho =$ constant)
- Newtonian fluid
- no gravity
- constant thermal properties ($\alpha =$ constant and $\nu =$ constant)
- no dissipation source in the energy equation

These assumptions infuence the simulation. The influence of these assumptions will be discussed in Section 6.

Conservation of mass is governed by the continuity equation:

$$\nabla \cdot \mathbf{U} = 0 \tag{3.1.1}$$

Conservation of momentum is governed by the momentum equation:

$$\frac{\partial \mathbf{U}}{\partial t} + \nabla \cdot (\mathbf{U}\mathbf{U}) - \nabla \cdot (\nu \nabla \mathbf{U}) = -\nabla p \tag{3.1.2}$$

Conservation of energy in a fluid is governed by the temperature equation for a fluid:

$$\frac{\partial T}{\partial t} + \nabla \cdot (\mathbf{U}T) = \nabla \cdot (\alpha_f \nabla T) \tag{3.1.3}$$

Conservation of energy in a solid is governed by the temperature equation for a solid:

$$\frac{\partial T}{\partial t} = \nabla \cdot (\alpha_s \nabla T) \tag{3.1.4}$$

Under these assumptions, the energy equation is decoupled from the momentum and continuity equation. Under this condition, it could also be called the passive scalar equation or the passive scalar heat equation. It is important to realize that the decoupling implies that the flow field is not influenced by the temperature. The temperature is passively convected by the flow. This yields the possibility to solve for multiple temperature fields during the same simulation [33].

3.2. Solving the Navier-Stokes equations with OpenFOAM and STAR-CCM+

This section is intended to give a general overview of the numerical method used. A complete derivation of the transport equation is given in appendix A. The fnite volume method in OpenFOAM and STAR-CCM+ is in general 2nd order accurate in space (depending on the convection differencing scheme (CDS) used, see Appendix A.3). Whenever possible the 2nd order linear CDS is used but sometimes order of accuracy had to be decreased to stabilize the simulation. The time-stepping algorithm is 2nd order accurate in time (see appendix A) and is implicit (backward Euler). Implicit timestepping is in general not used for a DNS, since the equations need to be solved iteratively. However, for practical reasons the backward Euler scheme was chosen. First of all it is readily available in OpenFOAM and STAR-CCM+. Second, the implicit scheme allows for high Courant-Friedrichs-Lewy condition (CFL). The CFL is defined using the velocity at the cell face ($\mathbf{U}_f$), the vector connecting the cell centers on either side of the face ($\mathbf{d}$) and the timestep (Δt):

$$CFL = \frac{\mathbf{U}_f \cdot \mathbf{d}}{\Delta t} \tag{3.2.1}$$

A high CFL is benificial when performing simulations using complex cells such as polyhydral cells. Meshes which use these cells will have small cells locally, at least when using the STAR-CCM+ mesher, leading to local high CFL.

OpenFOAM and STAR-CCM+ have small differences. In OpenFOAM the PISO-algorithm is used for iteratively solving the equations and in STAR-CCM+ the SIMPLE-algorithm is used. These algorithms will be described below. Furthermore, STAR-CCM+ provides the bounded-central scheme (see Appendix A.3), which was very useful performing simulations using polyhydral cells (see results in Section 4.6.2).

3.2.1. The PISO-algorithm

Since the equations are discretized implicitely in time (see Appendix A) they need to be coupled using a coupling algorithm. The algorithm used in OpenFOAM for unsteady simulations is the pressure-implicit split-operator algorithm, or PISO-algorithm. This algorithm was first proposed by Issa [17] and is described here for incompressible flow [13, 18].

The algorithm performs several steps:

- Predictor Step
- First corrector step
- Second corrector step

In the predictor step the pressure field at t^{n-1} is used to solve the momentum equation, resulting in an intermediate velocity field. This velocity field will in general not satisfy the continuity equation.

In the first corrector step a pressure equation is solved to obtain an intermediate pressure field. Using this pressure field the momentum equation is solved again, resulting in a new velocity field which satisfies the continuity equation.

In the second corrector step the first corrector step is repeated, yielding a final pressure and velocity field.

More corrector steps can be performed which will improve the order of accuracy. However, for two corrector steps the order of accuracy is generaly higher then the order of accuracy of the discretization in time of the incompressible Navier-Stokes equation. This is off course dependent on the order of the discretization in time.

3.2.2. The SIMPLE-algorithm

In STAR-CCM+ the semi-implicit method for pressure-linked equations, or SIMPLE-algorithm, is used for the coupling of equations [13, 32].

In the predictor step the pressure field at t^{n-1} is used to solve the momentum equation, resulting in an intermediate velocity field. This velocity field will in general not satisfy the continuity equation.

In the first corrector step a pressure correction equation is solved to obtain an correction for the pressure field. The pressure field is updated using this correction and using under-relaxation.

The velocity field is updated using the correction for the pressure field.

Iterature this procedure until the fields do not change anymore (within a certain tolerance).

3.2.3. Treatment of non-linearity

The non-linearity in the momentum equation is lagged in OpenFOAM. The non-linear term in the momentum equations is treated as follows (A.2.14):

$$\int_{V_P} \nabla \cdot (\mathbf{U}\mathbf{U}) dV = \sum_f F\mathbf{U}_f \tag{3.2.2}$$

The face-fluxes (which contain the velocity) F are taken from the previous timestep, thereby linearizing the equation.

3.3. Description of different cell types used

During this thesis three different cell-types will be used. Hexahedral cells, extruded polyhydral cells and full polyhydral cells. This section will explain the difference between the three different cells types. First, the 2D variant of the hexahedral cell, the square, and the 2D variant of the polyhdral cell, the polygon, will be shown in Figure 3.1. Theses 2D shapes will be expanded into their 3D variants. The square is extruded normal to its surface, creating a hexahedral cell as can be seen in Figure 3.2. The polygon can be transformed into a 3D cell in two ways. If the polygon is extruded normal to its face an extruded polydydral cell will be created, as can be seen in Figure 3.3. It can also be expanded as an arbitrary shape, creating a general polyhdron, as can be seen in Figure 3.3.

Furthermore, geometries in this thesis are meshed using a prism layer. A prism layer is a layer of cells extending from the surface of a geometry. All prism layers have a stretching ratio (SR). This means that the cells are stretched in wall-normal direction using the stretching ratio. For instance a stretching ratio of 2.0 means that a layer of cells in the prism layer has a heigth twice as much as the previous layer. Sometimes the prism layer fills the entire domain, sometimes it is stopped at a certain wall-normal distance. The rest of the domain is then differently meshed. The mesh which is not

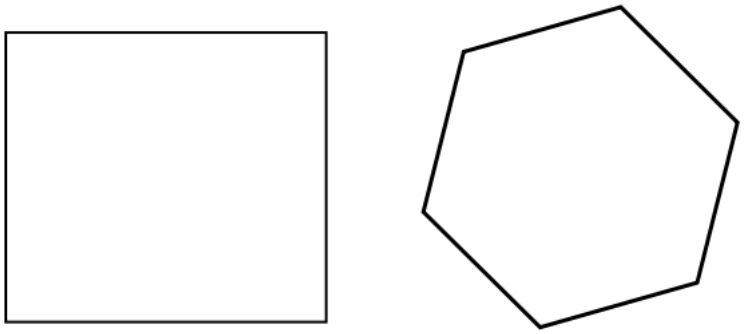

Figure 3.1.: 2D cells. On the left a square can be seen. On the right a polygon (in this case a hexagon).

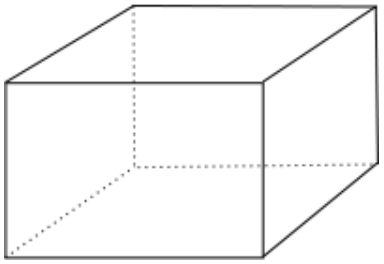

Figure 3.2.: A 3D hexahedral cell.

in the prism layer is called the bulk region mesh. A prism layer and bulk region are visualized in Figure 3.4.

3.4. A discussion of the numerical method used

The drawback of the numerical method used is not only the relatively low order of accuracy (compared to spectral methods or high-order finite difference method) but also the use of colocated grids and the use of implicit time-stepping.

Let us first discuss the use of a colocated grid. If one needs to use an off-the-shelf solver there is no way around this to my knowledge. OpenFOAM, Star-CCM+ and Fluent all use colocated grids. The influence of the use of colocated grids is neatly analyzed in [12] and [34]. And this thesis is not the first work to test this method for direct numerical simulations of a channel flow [30].

Felten and Lund [12] descibe the errors originating from the use of the colocated arrangement. The pressure correction (such as PISO) leads to an error in the divergence of the velocity field. This error can be controlled by using a fine mesh (neccesary for a DNS anyway) and increasing the number of pressure corrections. The second error originates from the conservation of kinetic energy, this is associated with the interpolation used to interpolate cell-center values to cell-faces. This error can be eliminated (see appendix B) at the cost of decreasing the accuracy of the interpolation.

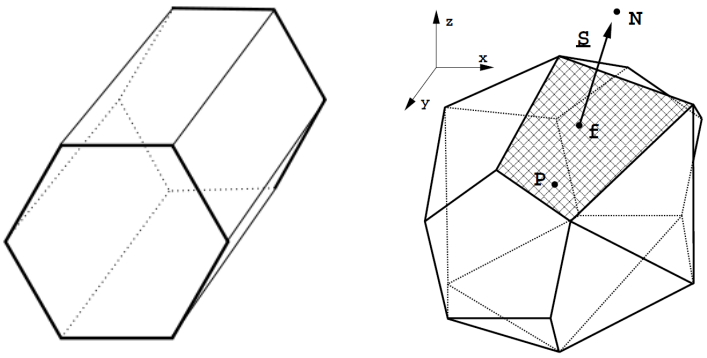

Figure 3.3.: The two 3D types of polyhydral cells used in this thesis. On the left an extruded polydyral cell can be seen, on the right a full polyhydral cell can be seen.

The paper by Schmid et.al. [30] shows that good accuracy can be obtained using colocated meshes in combination with a pressure-correction approach for timestepping, for the simulation of the turbulent channel flow. Even when a few percent of upwind is used (blended convection differencing scheme).

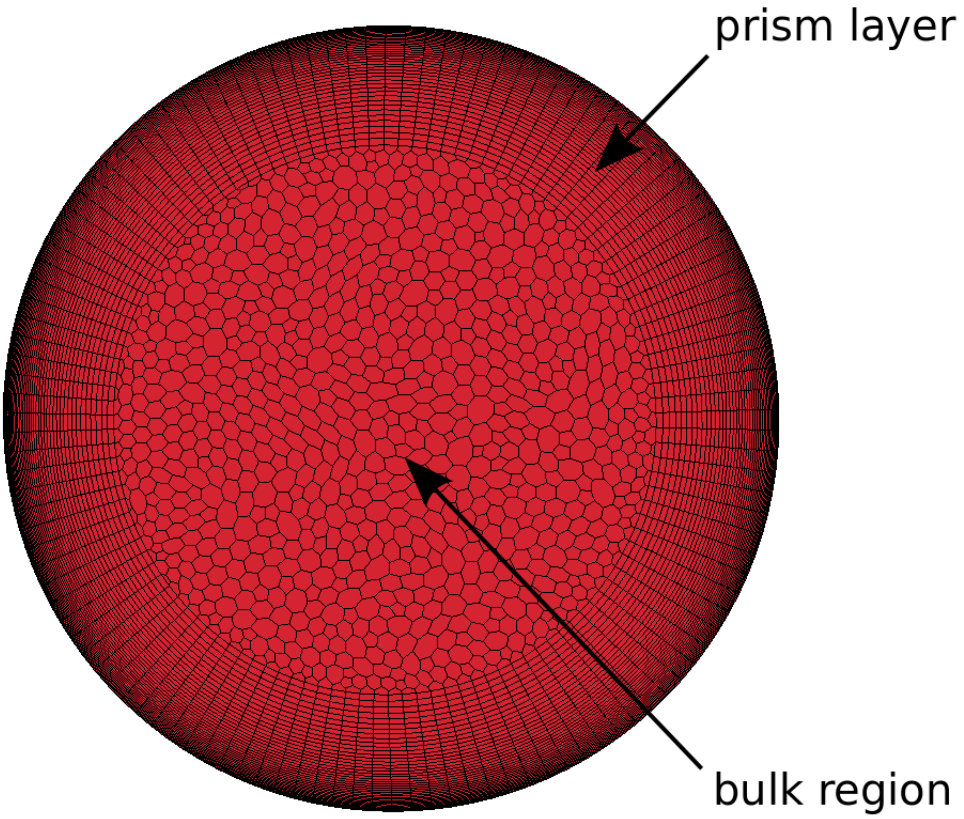

Figure 3.4.: A slice of a mesh used to mesh a pipe geometry. The prism layer can be seen. In the prism layer it can be seen that cells are stretched in wall-normal direction. The bulk region can also be seen.

4. Direct numerical simulation of channel and pipe flow

This chapter will present the most important results in this thesis. Two of the main objectives of the thesis will be achieved in this thesis. The DNS accurracy of OpenFOAM and STAR-CCM+ for channel and pipe flows will be assessed in general, as well as for the complex cell types, which were seen in section 3.3.

Before results can be presented the famous channel and pipe flows will be explained in section 4.1. The simulations must be started using an initial field that ensures quick development of the flow, as explained in section 4.2. Since both the channel and pipe flow are periodic in streamwise direction the pressure and temperature require a special treatment, which will be explained in section 4.3. It is customary to compare results for channel or pipe flow with a reference. A closer look into these references will be provided in section 4.4. Next, the results for channel and pipe flows are presented. In Section 4.5.1 results for the channel flow with non-conjugate heat transfer will be presented, followed by the results with conjugate heat transfer in Section 4.5.2. In Section 4.6 results for the pipe flow will be presented. The results for the pipe flow will be presented for both extruded polyhydral cells (Section 4.6.1) and full polyhydral cells (Section 4.6.2). This chapter will be closed in section 4.7 with the conclusions for the two first objectives of this thesis.

4.1. Introduction to channel and pipe flow

The turbulent channel (or pipe) flow is often referred to as a canonical flow case, since it is one of the most simple wall-bounded flows one can think of. Therefore, this test case is suitable to verify if a numerical solver is able to accurately predict the fluctuations at the wall. Furthermore, a lot of reference solutions are available to compare solutions with.

The flow one whishes to investigate is a fully-developed turbulent wall-bounded flow. Fully-developed means transient effects, for instance due to inlets or outlets have died out. A flow suitable for such investigation is the flow between two infinite parallel plates, or the flow in a pipe of infinite length. For practical purposes the infinite plates are truncated in streamwise (x) and spanwise (z) direction yielding the channel flow as seen on the left in Figure 4.1, the infinitely long pipe is truncated in axial (x) direction as seen on the right in Figure 4.1. Periodic boundary conditions are used to simulate infinite geometrical conditions.

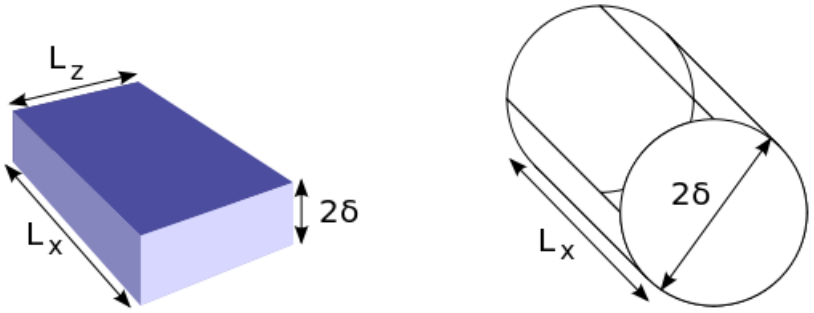

Figure 4.1.: The configuration of the channel and pipe flow. The channel is periodic in x and z direction, as seen on the left. The pipe is periodic in x direction, as seen on the right.

The Reynolds number describing the turbulent channel (or pipe) flow is often defined based on the channel half-height (or radius of the pipe) δ and friction velocity u_τ:

$$Re_\tau = \frac{u_\tau \delta}{\nu} \tag{4.1.1}$$

4.2. Inititial conditions for channel and pipe flows

The initial flow field must ensure the development of a fully developed turbulent channel flow. In this thesis the initial fields were always taken as instantaneous fields from a previous simulation.

Since such a flow field is not always available other initial fields are usefull. The standard intial field available for OpenFoam is created by Eugene de Villiers [10]. This initial condition is inspired by the streak-instability cycle, described in Section 2.4. The initial fields is based in the parabolic laminar profile. Low-speed and high-speed streaks are superimposed on the laminar profile at $y^+ = 12$. These streaks are superimposed with a sinusoidal perturbation at the interface between the streaks.

If an initial field for the temperature is not available, but an initial field for the flow is, the initial field for the temperature can be created based on the flow field. As can be seen in Figure 4.7, the mean profile of the temperature resembles the mean profile of the streamwise velocity, and the profile of T_{rms} resembles the profile of u_{rms}. Thus scaling the streamwise component of a fully developed flow fields generates an appropiate initial field for the temperature.

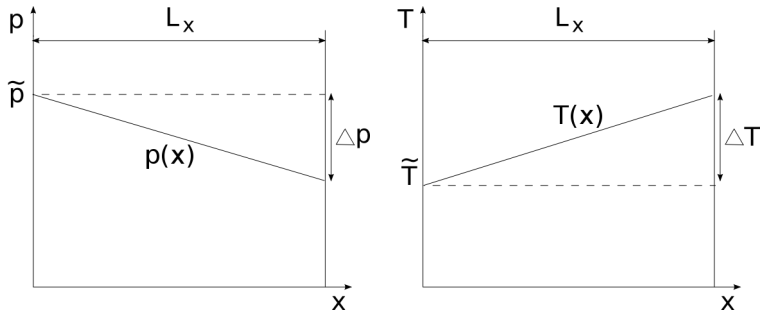

Figure 4.2.: Periodicity in the pressure and temperature for the channel and pipe flow. The pressure and temperature are split into a periodic part, and a non-periodic part.

4.3. Periodicity of the turbulent channel and pipe flow

Both the turbulent channel and pipe flow are periodic in streamwise direction. However, in general the pressure and the temperature will not be periodic. The pressure will drop in streamwise direction to overcome the drag from the wall. The temperature will increase (or decrease) due to the heat flux from (or to) the fluid to (or from) the wall, this can be seen in Figure 4.2. Therefore, both the pressure and the temperature field will be split into a fluctuating periodic part, and a non-periodic part [3]. The non-periodic part is not constant, the gradient of the non-periodic part is constant.

The pressure is split into the periodic pressure $\tilde{p}$ and the non-periodic pressure $\frac{\Delta p}{L_x}x$. The pressure drop over the channel (or pipe) is given by Δp and L_x is the lenght of the domain:

$$p = \tilde{p} + \frac{\Delta p}{L_x}x \tag{4.3.1}$$

Since the pressure decreases linearly a constant pressure gradient can be introduced:

$$p = \tilde{p} + \frac{dp}{dx}x \tag{4.3.2}$$

The periodic pressure can be introduced into the source term in the momentum equation. The resulting momentum equation is:

$$\frac{\partial \mathbf{U}}{\partial t} + \nabla \cdot (\mathbf{U}\mathbf{U}) - \nabla \cdot (\nu \nabla \mathbf{U}) = -\nabla \tilde{p} - \frac{dp}{dx} \cdot (1, 0, 0) \tag{4.3.3}$$

The pressure gradient $\frac{dp}{dx}$ can be related to the friction velocity using the balance of mean forces in axial direction. The resulting relation for the channel is [28]:

$$u_\tau = (-\frac{\delta}{\rho}\frac{dp}{dx})^{1/2} \tag{4.3.4}$$

A similar analysis for the pipe flow yields the following relation [28]:

$$u_\tau = (-\frac{\delta}{2\rho}\frac{dp}{dx})^{1/2} \tag{4.3.5}$$

For the temperature field the situation in which the temperature can develop as in Figure 4.2 is analyzed. The temperature can only increase in this way if the heat flux from the wall into the fluid is constant. This could be achieved by specifying a constant heat flux. However in literature this is achieved by specifying a linear increase in wall temperature in streamwise direction [21, 29, 33]. Thus the temperature increase as shown in Figure 4.2 is both the temperature increase at the wall and the mean temperature increase of the fluid.

The temperature field is split similar to the pressure field:

$$T = \tilde{T} + \frac{\Delta T}{L_x}x \tag{4.3.6}$$

An expression needs to be found for $\frac{\Delta T}{L_x}$. This expression is derived in the following equations. The time it takes for the fluid to pass through the channel is given by:

$$t_1 = \frac{L_x}{u_{bulk}} \tag{4.3.7}$$

The amount of heat transferred to the fluid during this time is given by:

$$mc_p\Delta T = 2q_w L_x L_z t_1 \tag{4.3.8}$$

In this expression the internal energy increase is given by $mc_p\Delta T$ where m is the mass in the channel. The heat flux from the wall to the fluid is given by q_w, the surface of the wall is given by the product of the length L_x of the channel and the width of the channel L_z

Inserting the amount of mass in the channel and using 4.3.7:

$$\rho 2\delta L_x L_z c_p \Delta T = 2q_w L_x L_z \frac{L_x}{u_{bulk}} \tag{4.3.9}$$

Now the temperature gradient can be expressed as:

$$\frac{\Delta T}{L_x} = \frac{q_w}{\delta \rho c_p u_{bulk}} \tag{4.3.10}$$

The splitting of the temperature field can now be rewritten:

$$T = \tilde{T} + \frac{q_w}{\delta \rho c_p u_{bulk}} x \tag{4.3.11}$$

When the split temperature field is inserted into the energy equation (equation 3.1.3), the equation for the energy equation governing the periodic temperature field is obtained. The right hand side of the split temperature field drops out of the energy equation everywhere, except for the derivate with respect to x originating from the convective term. This term will end up as a source term:

$$\frac{\partial \tilde{T}}{\partial t} + \nabla \cdot (\mathbf{U}\tilde{T}) = \nabla \cdot (\alpha_f \nabla \tilde{T}) - u \frac{q_w}{\delta \rho c_p u_{bulk}} \tag{4.3.12}$$

A similar analysis can be performed for the pipe yielding:

$$\frac{\partial \tilde{T}}{\partial t} + \nabla \cdot (\mathbf{U}\tilde{T}) = \nabla \cdot (\alpha_f \nabla \tilde{T}) - u \frac{2q_w}{\delta \rho c_p u_{bulk}} \tag{4.3.13}$$

The boundary condition is also split in a periodic and constant part for the simulation without conjugate heat transfer. Since the simulation solves for the periodic temperature field, the periodic part must also be aplied as a boundary condition. Thus the wall temperature must be set to T_w.

In the simulations with conjugate heat transfer the wall is of course not set to a constant temperature. The temperature field in the solid is made periodic in a similar manner as for the fluid. The sign of the source is reversed to conserve energy. The equation solved for in the solid than becomes [33]:

$$\frac{\partial \tilde{T}}{\partial t} = \nabla \cdot (\alpha_s \nabla \tilde{T}) + u \frac{2q_w}{d \rho c_p u_{bulk}} \tag{4.3.14}$$

4.4. Reference databases for pipe and channel flows

Throughout this thesis, results will be compared to several reference databases. Before doing this comparison , it is good to take a moment te see what is available and compare it with eachother. All the reference databases used are summarized in Table 4.1.

Before comparing references with eachother, it must be described what is visible in the figures comparing the results. Throughout this thesis the same format will be used for presenting the results. This format can be seen for instance in Figure 4.3. At the top of Figure 4.3 the mean streamwise velocity can be seen, plotted versus the wall-normal distance. The wall-normal distance is normalized using (2.3.3) and the velocity using (2.3.4). It is customary to plot the mean streamwise velocity versus the wall-distance using a logarithmic scale on the y^+-axis. At the bottom of Figure 4.3, the root-mean-squares of the velocity fluctuations in all three directions can be seen. The three different directions are indicated in the figure by u,v and w for the x,y, and z-direction. The fluctuations are also scaled using (2.3.4). The format used for presenting the results in the pipe geometry is very similar. The three components for the pipe geometry are denoted using u_z,u_r and u_θ for the z, r, and θ-direction.

The references for the channel flow at $Re_\tau = 180$ (see Figure 4.3) will be analyzed first. As can be seen small differences are present when comparing the reference solutions with eachother. The most striking differences occur in the middle of the channel for the mean flow (at $y^+ = 180$), and in the peak of the u_{rms} profile. Furthermore, it is strange to see that results by Jiminez extend beyond $y^+ = 180$, since by definition this is the center of the channel. To quantify the difference between the references, values for the peak in u_{rms} are compared in Table 4.2. The difference between the value of the peak in u_{rms} is largerst between the results of Kim & Moin and Kawamura (250 million points).

Secondly, the references for the channel flow at $Re_\tau = 150$ (see Figure 4.4) will be analyzed. The root-mean-squares of the fluctuations of Saad and Tiselj agree very well with eachother. Tiselj underestimates the mean flow slightly with respect to Kawamura.

Thirdly, the references for the pipe flow (see Figure 4.5) will be analyzed. Some variation in the peak values of $u^+_{z,rms}$ is present just as for the channel flow. Especially the fact the the peak value of the $u^+_{z,rms}$ obtained by Saad is lowest of the three references is striking, since the results of Saad were obtained for $Re_\tau = 185$ and the results for Eggels and Kasagi were obtained for $Re_\tau = 180$. It is well known that the peak in $u^+_{z,rms}$ is larger for higher Reynolds numbers. Another striking difference is the difference in results for $u^+_{z,rms}$ in the center of the pipe ($y^+ = 160 - 180$). Saad underestimates $u^+_{z,rms}$ in the center of the pipe with respect to Kasagi and Eggels.

It is important to remember that small differences are present between reference solutions. Thus, if results match perfectly with one reference this automatically means that it does not match perfectly with another reference.

Table 4.1.: The different references used in this thesis. Different references are denoted by their names. The difference between the Kawamura references for $Re_\tau = 180$ is indicated by the size of the mesh in millions. The superscripts next to the Reynolds numbers indicate if heat transfer (HT) or conjugate heat transfer (CHT) was taken into account in the reference. The order of accuracy in space of the method is written in brackets behind the method. Multiple cell sizes (for instance $0.05 - 4.4$) indicate growth from the wall to the center of the geometry. Starred cell sizes (*) indicate number of cells/points if this was reported instead of cell sizes. Domain size is given in x, z and y direction for channels, and r and z direction for pipes.

Reference	**Geom.**	Re_τ	**Method**	Δx^+, Δz^+, Δy^+	**Domain**	**Source**
Kim and Moin	channel	180	spectral	12, 7, 0.05-4.4	4 π,2 π, 2	http://turbulence.ices.utexas.edu/
Kawamura 1m	channel	180^{HT}	FDM (2nd)	9, 4.5, 0.4-11.5	6.4,3.2,2	http://murasun.me.noda.tus.ac.jp/turbulence/
Kawamura 8m	channel	180^{HT}	FDM (2nd)	4.5, 2.25, 0.2-5.9	6.4,3.2,2	http://murasun.me.noda.tus.ac.jp/turbulence/
Kawamura 250m	channel	180^{HT}	FDM (4th)	1.1, 1.1, 0.05-0.97	6.4,3.2,2	http://murasun.me.noda.tus.ac.jp/turbulence/
Kawamura 500m	channel	180^{HT}	FDM (4th)	0.56, 1.1, 0.05-0.97	6.4,3.2,2	http://murasun.me.noda.tus.ac.jp/turbulence/
Jiminez	channel	180	spectral	9, 6.7, 97*	12 π,4 π, 2	http://torroja.dmt.upm.es/ftp/channels
Tiselj	channel	150^{CHT}	spectral	128*, 65*, 97*	5 π, π, 2	private communication
Kawamura	channel	150	FDM (2nd)	7.5, 3.75, 0.17-4.94	12.8, 6.4, 2	http://murasun.me.noda.tus.ac.jp/turbulence/
Reference	**Geom.**	Re_τ	**Method**	Δr^+, Δz^+, $\Delta \theta^+$	**Domain**	**Source**
Saad	pipe	180^{HT}	FDM (2nd)	129*, 129*, 257*	2,15	private communication
Kasagi	pipe	180	FDM (2nd)	0.46-2.99, 7.03, 8.84-0.05	2,10	http://www.thtlab.t.u-tokyo.ac.jp/
Eggels	pipe	180	FVM (2nd)	1.88, 7.03, 8.84-0.05	2,10	http://www.thtlab.t.u-tokyo.ac.jp/

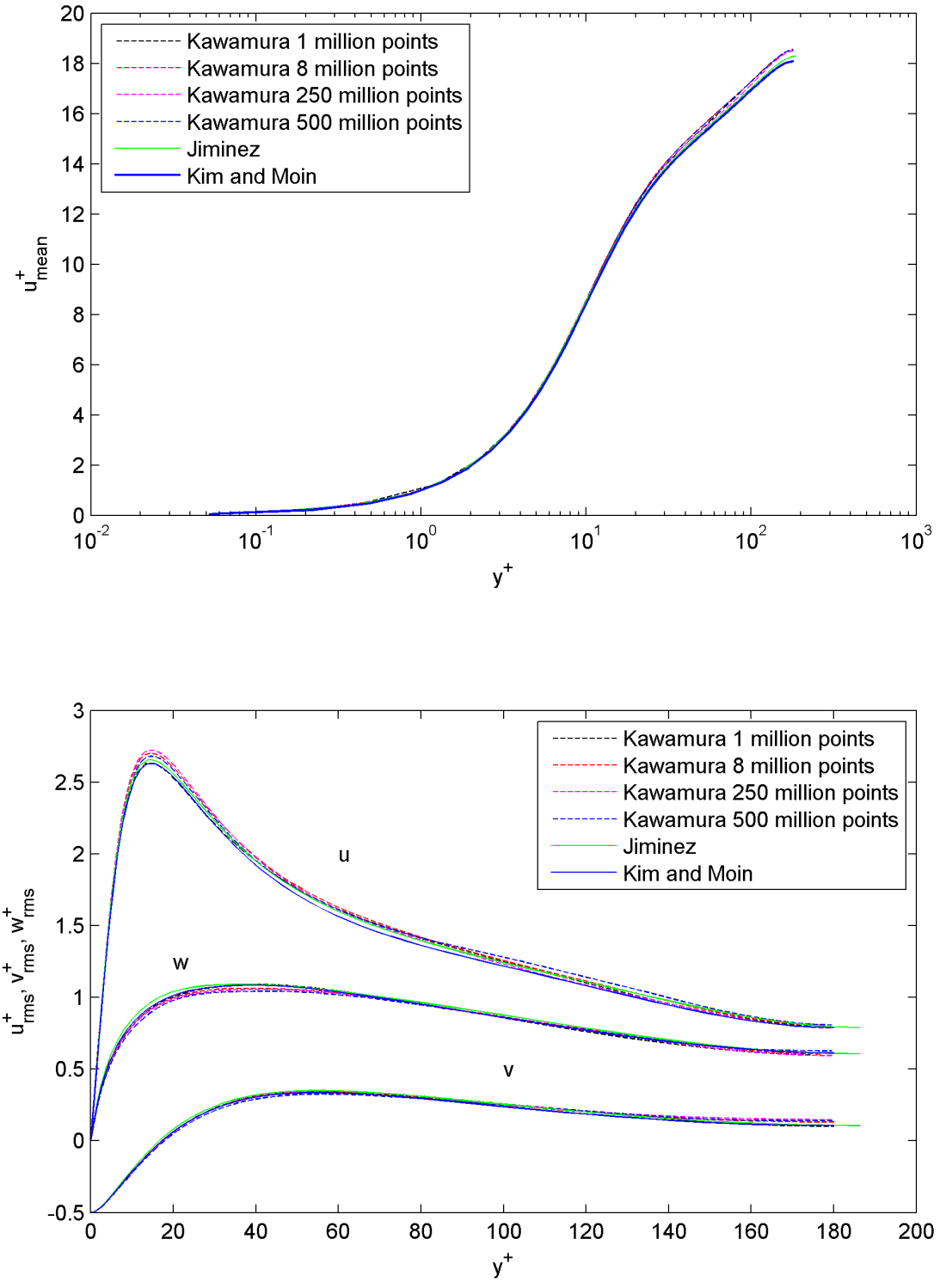

Figure 4.3.: Different references compared for the channel flow at $Re_\tau = 180$. As can be seen there is a small spread between the different results. Differences are quantified in Table 4.2. Results for v^+_{rms} translated by -0.5 for visibility.

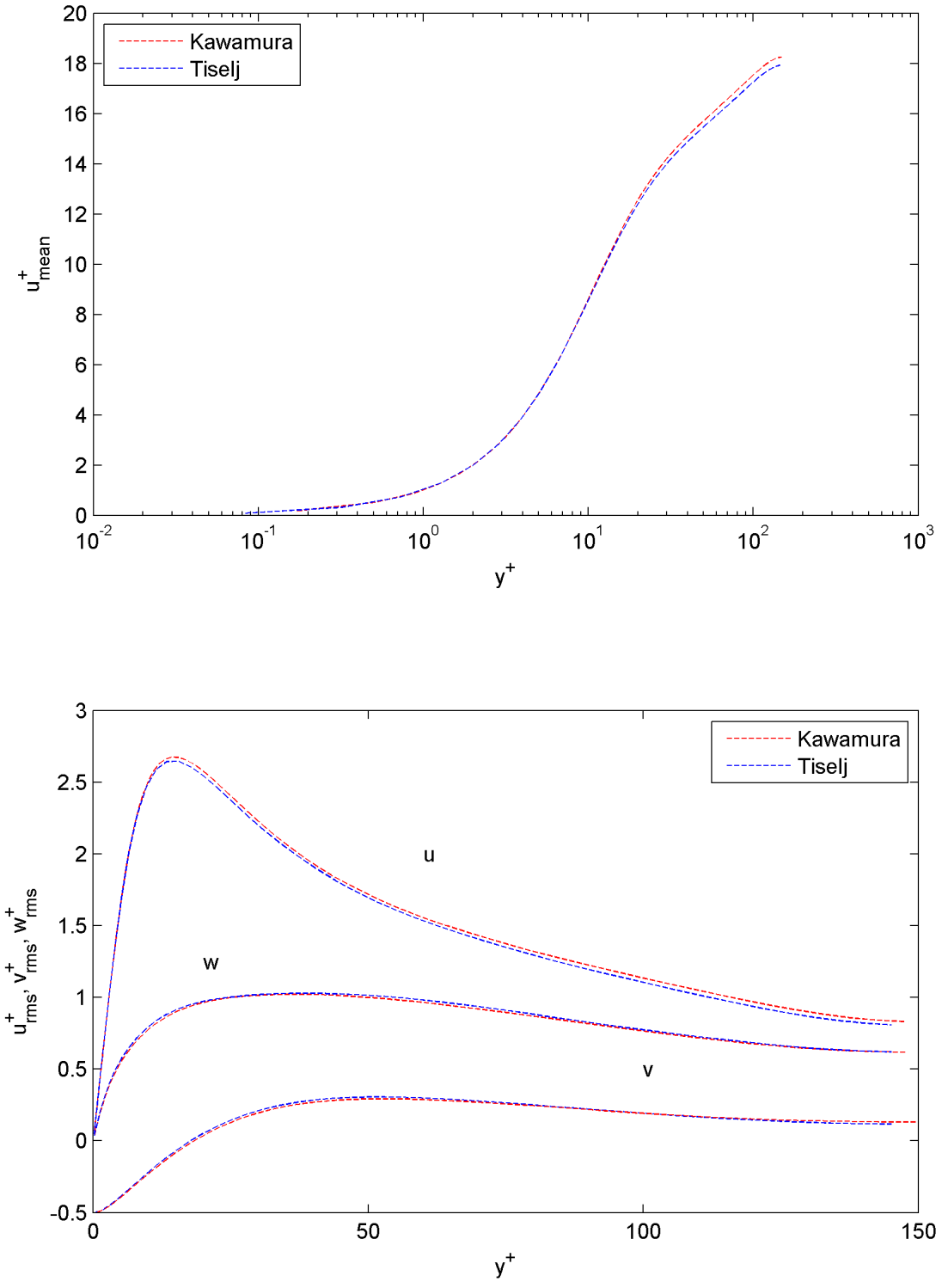

Figure 4.4.: Different references compared for the channel flow at $Re_\tau = 150$. Agian there is a small spread between the different results. Results for v^+_{rms} translated by -0.5 for visibility.

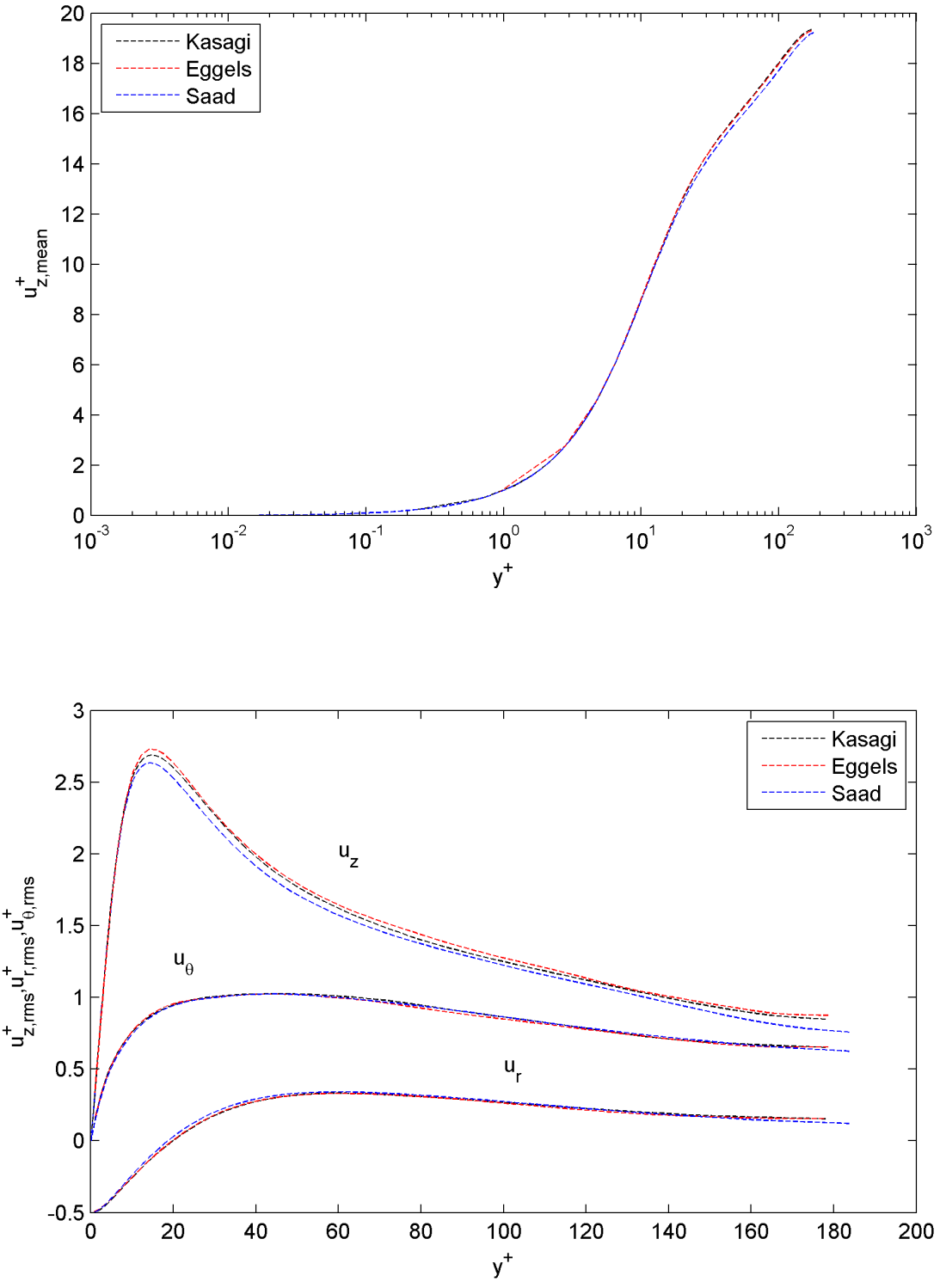

Figure 4.5.: Different references compared for the pipe flow at $Re_\tau = 180$. As can be seen there is a small spread between the different results. Results for $u^+_{r,rms}$ translated by -0.5 for visibility.

Table 4.2.: Comparison of the maximum values (the peak around $y^+ = 12$) of the u^+_{rms} for the different reference solutions, references for the channel flow at $Re_\tau = 180$ compared. See Figure 4.3.

Reference	**Peak in u_{rms}**	**Relative difference w.r.t. Kim & Moin**
Kawamura 1 million points	2.6300	0.1%
Kawamura 8 million points	2.7026	2.8%
Kawamura 250 million points	2.7227	3.6%
Kawamura 500 million points	2.6805	2.0%
Jiminez	2.6591	1.2 %
Kim & Moin	2.6283	0 %

4.5. DNS results for channel flow

In this section results for the turbulent channel flow will be presented. First results for the channel flow with non-conjugate heat transfer will be presented in Section 4.5.1. Second, the results for channel flow with conjugate heat transfer will be presented in Section 4.5.2.

4.5.1. DNS results for channel flow with non-conjugate heat transfer

As a first step to test the accuracy of the OpenFOAM and Star-CCM+ codes, a channel flow simulation was performed. The computational details can be seen in table 4.3:

Table 4.3.: The computational details of the channel flow, including non-conjugate heat transfer.

Re_τ	180
Pr	$0.71, 1, 2$
number of cells (x,z,y)	2.1 million (128x128x128)
domain (x, z, y), (x^+, z^+, y^+)	6.4, 3.2, 2 meters, 1152, 576, 360
mesh Δx^+, Δz^+, Δy^+	9, 4.5, 0.4-8.9
Δt, Δt^+	6 s, 0.00108
SR	1.05
CDS	linear
PISO corrections	4

As can be seen in the list of computational details three different temperature fields are solved for using three different Prandtl numbers. The Prandtl numbers were chosen since these Prandtl numbers were available as reference solutions, the same holds for the Reynolds number. The domain and mesh was chosen to resemble the domain and mesh used by Kawamura [16], except for the fact that more cells were used in the wall-normal direction. The final mesh and time step are the result of a sensitivity analysis. The start-up and averaging procedure are the results of a sensitivity analysis. The initial field was taken from a previous simulation and was fully developed. Five non-dimensional times ($5t^+$) (2.3.7) were used for start-up and were neglected when statistics were obtained.

Statistics were obtained during $30t^+$ (2.3.7). In OpenFOAM statistics were obtained using ensemble averaging over 151 fields which were seperated in time by $0.2t^+$. In STAR-CCM+ statistics were obtained using a running time average.

In OpenFOAM the channel flow including heat transfer was simulated, in STAR-CCM+ the channel flow without heat transfer was simulated.

The results for the flow obtained with OpenFOAM can be seen in Figure 4.6. Compared to the reference of Kawamura the mean is slighlty underpredicted. The root-mean-squares are also slightly underpredicted.

The results for the temperature obtained with OpenFOAM can be seen in Figure 4.7. The values for T^+_{rms} are strongly underpredicted here. However it must be remembered that results obtained with OpenFOAM are compared with the Kawamura 250 million points reference. It was seen in Section 4.4 that the peak in u^+_{rms}, which is stronlgy related to the peak in T^+_{rms}, in the Kawamura 250 million point solution is highest compared to the other references. The Kawamura 250 million points solution was used because this reference had a solution for all three Prandtl numbers available.

The results for the flow obtained with STAR-CCM+ can be seen in Figure 4.8. It can be seen that these results are slighlty beter than the results obtained with OpenFOAM.

For the channel flow simulation the dissipation rate of the turbulent kinetic energy (2.2.5) is also calculated (see Figure 4.9). It can be seen in Figure 4.9 that less dissipation is calculated using OpenFOAM compared to Kawamura. It is not the intention of this thesis to calculate budget terms for the turbulent kinetic energy correctly, but this is a good indication for the validity of the claim that a DNS (which should calculate all the dissipation of a flow) is performed in this thesis.

For the channel very little difference was found between the results obtained using OpenFOAM or STAR-CCM+, both for the mean velocity plots and the plots containing the fluctuations.

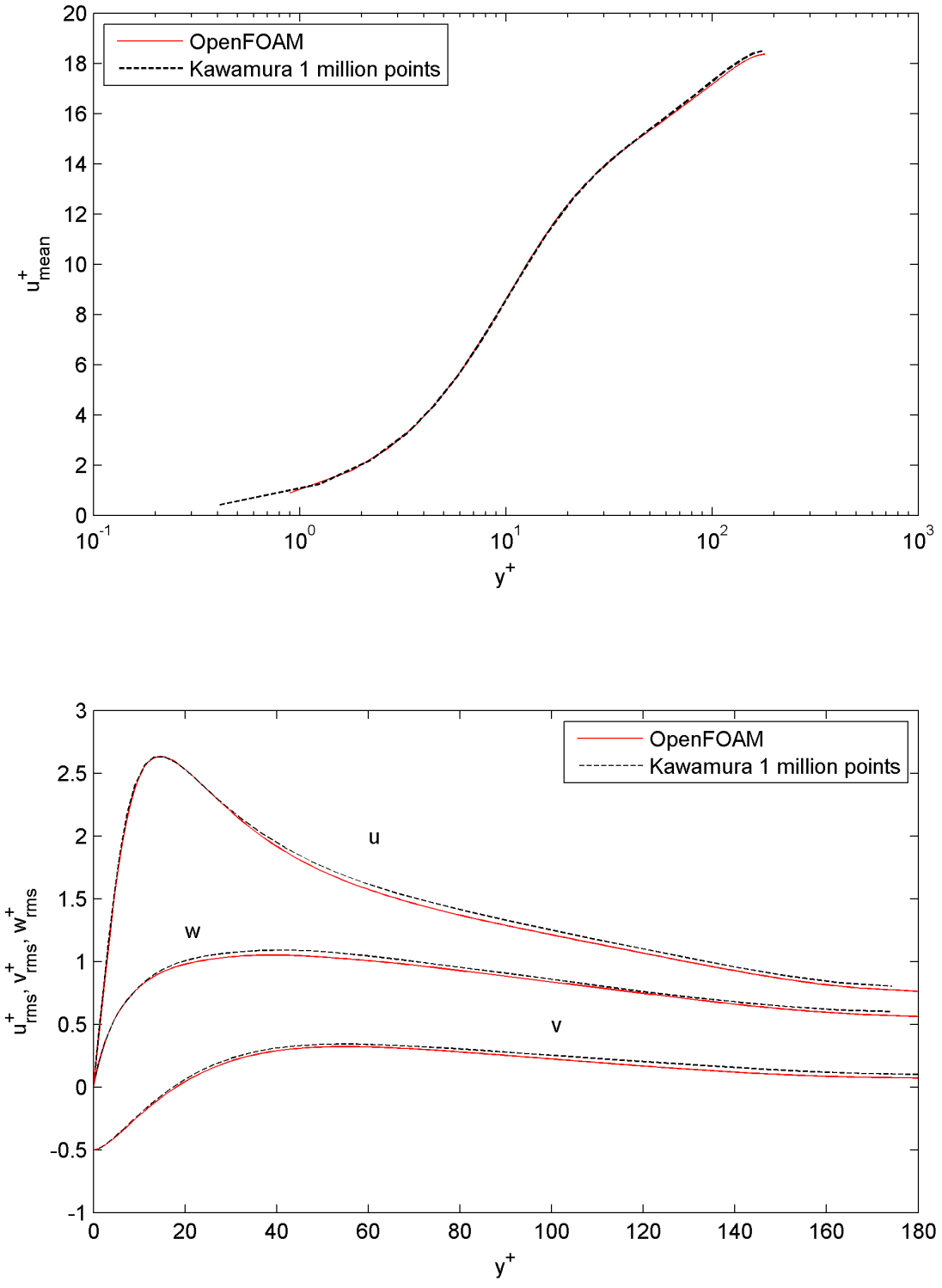

Figure 4.6.: Results for the velocities obtained with OpenFOAM. Results for the channel flow at $Re_\tau = 180$ are shown. Results for v^+_{rms} translated by -0.5 for visibility.

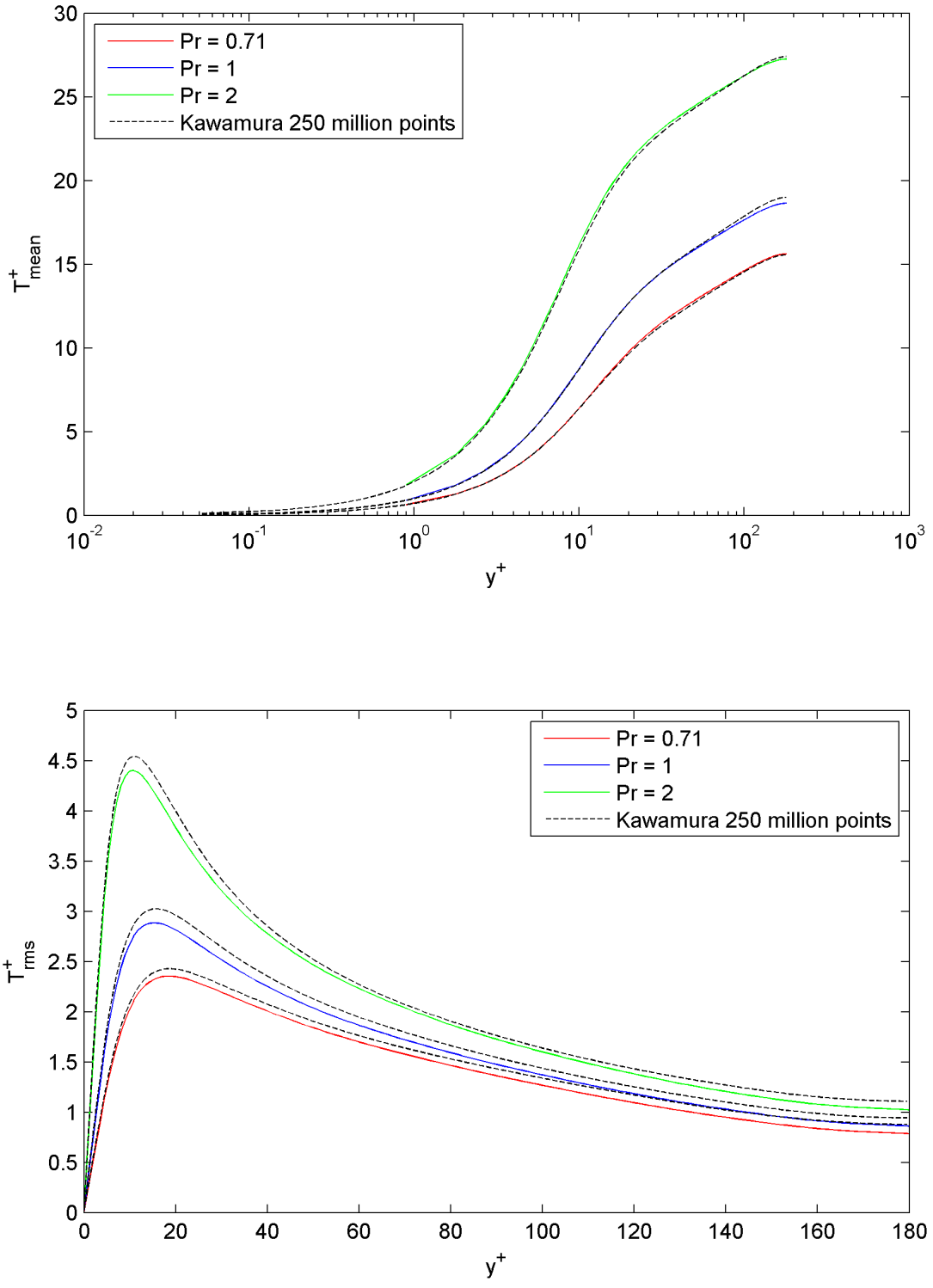

Figure 4.7.: Results for the non-conjugate heat transfer obtained with OpenFOAM. Results for the channel flow at $Re_\tau = 180$ are shown. Results for three different Prandtl numbers are shown.

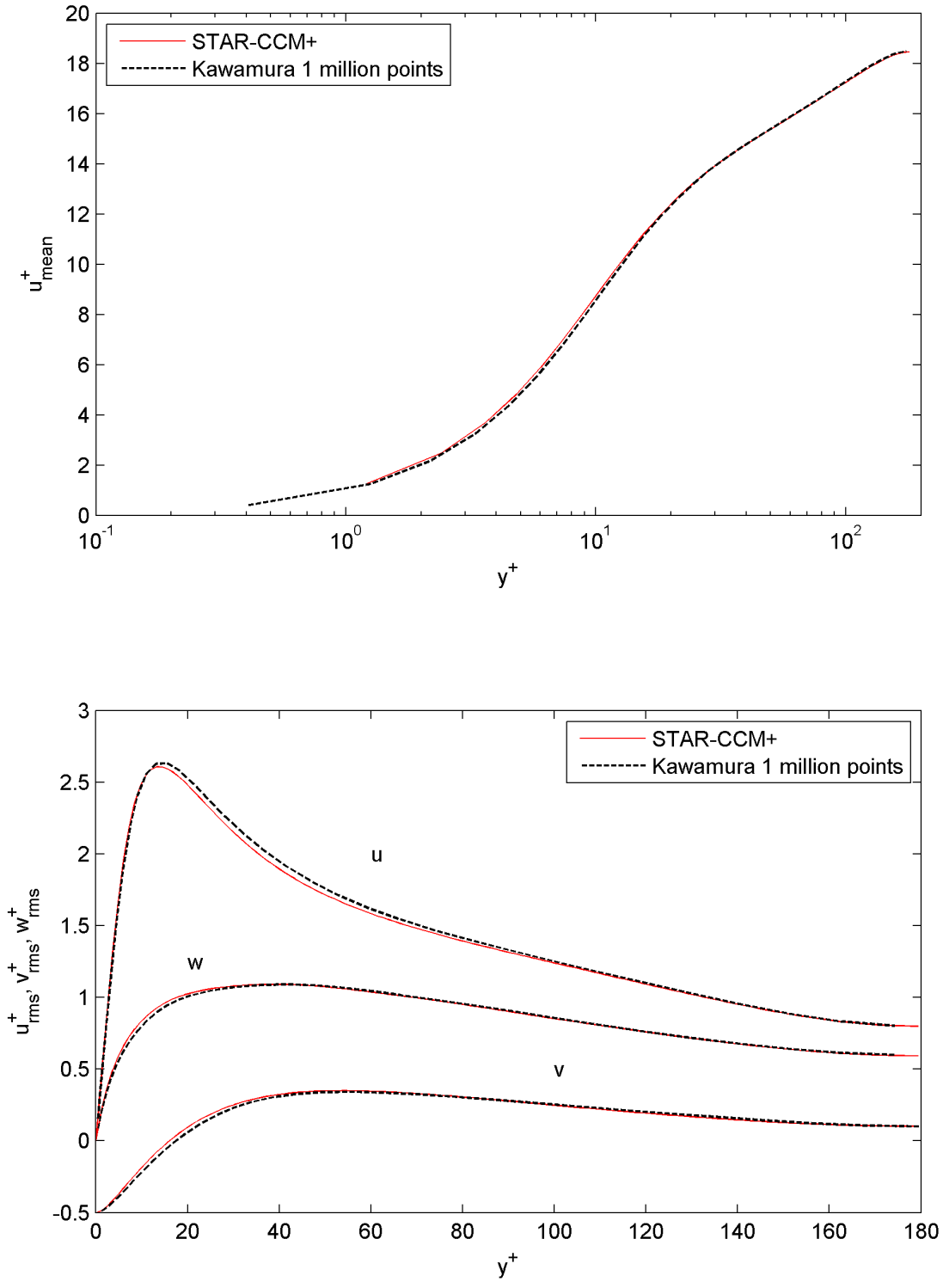

Figure 4.8.: Results for the velocities obtained with STAR-CCM+. Results for the channel flow at $Re_\tau = 180$ are shown. Results for v^+_{rms} translated by -0.5 for visibility.

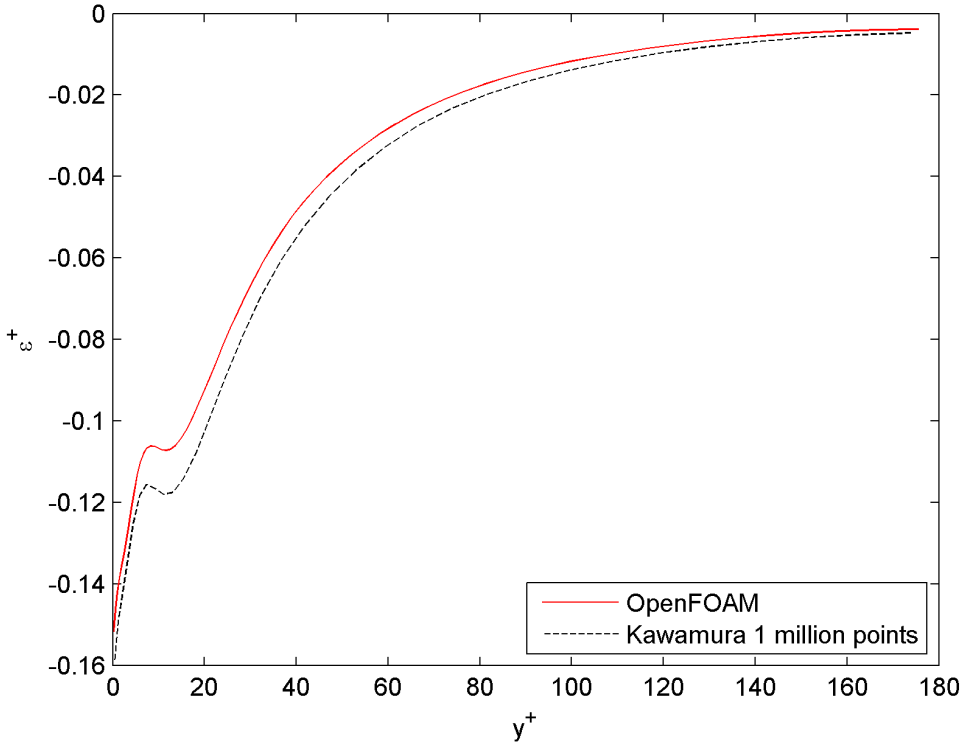

Figure 4.9.: Dissipation rate of the turbulent kinetic energy for the channel flow at $Re_\tau = 180$. Results obtained with OpenFOAM.

4.5.2. DNS results for channel flow with conjugate heat transfer

The computational details of the simulation with conjugate heat transfer can be seen in Table 4.4.

Table 4.4.: The computational details of the channel flow, including conjugate heat transfer.

Re_τ	150
Pr	0.71
K	1
d^{++}	1
dt	6 s (max CFL +/- 0.5), $dt^+ = 0.0009$
number of cells	2.0 million
domain (x, z, y), (x^+, z^+, y^+)	6.4, 3.2, 2 meters, 960, 478, 300
mesh Δx^+, Δz^+, Δy^+	7.5, 3.8, 0.3-7.4
SR	1.05
CDS	linear
PISO corrections	4

The smaller friction Reynolds number was chosen since the reference simulation was performed at this Reynolds number [33]. For the same reason the Prandtl number of 0.71 was chosen. The combination of the activity ratio and the wall thickness was

arbitrarily chosen out of the 40 cases provided by Tiselj [33]. The results can be seen in see Figures 4.11 , 4.12 and 4.10.

The simulation with conjugate heat transfer shows less accuracy than the simulation without conjugate heat transfer, when comparing the mean and root-mean-squares of the velocities (compare Figure 4.10 with Figure 4.6). This is not what one would expect since the mesh was finer and the timestep smaller with respect to the simulation without conjugate heat transfer (comparing non-dimensional cell sizes and non-dimensional timestep in Table 4.4 and Table 4.3). However, both references for the channel flow at Re_τ used a larger domain (see Table 4.1). This makes sense since the smaller Reynolds number will yield a slower drop of the two-point correlation in space. The domain size for a channel flow is generally selected such that the two-point correlations become close to zero halfway between the periodic interfaces, this is done to prevent influence of the inflow on the outflow.

The accuracy for the temperature is similar to the accuracy for the velocties (see Figure 4.11 for the temperature plots in the fluid, and Figure 4.12 for the temperature in the solid wall). The results for the fluctuations in the temperature in Figure 4.12 might look strange since it is simply a straight line. This result is obtained because of the thin solid wall ($d^{++} = 1$).

But perhaps the most interesting results for the conjugate heat transfer are shown in Figure 4.13. In this figure the correspondence between the velocity streaks in the fluid and the thermal streaks on the wall can be seen. It can be clearly seen that the low-speed streaks are reflected on the wall as hot thermal streaks.

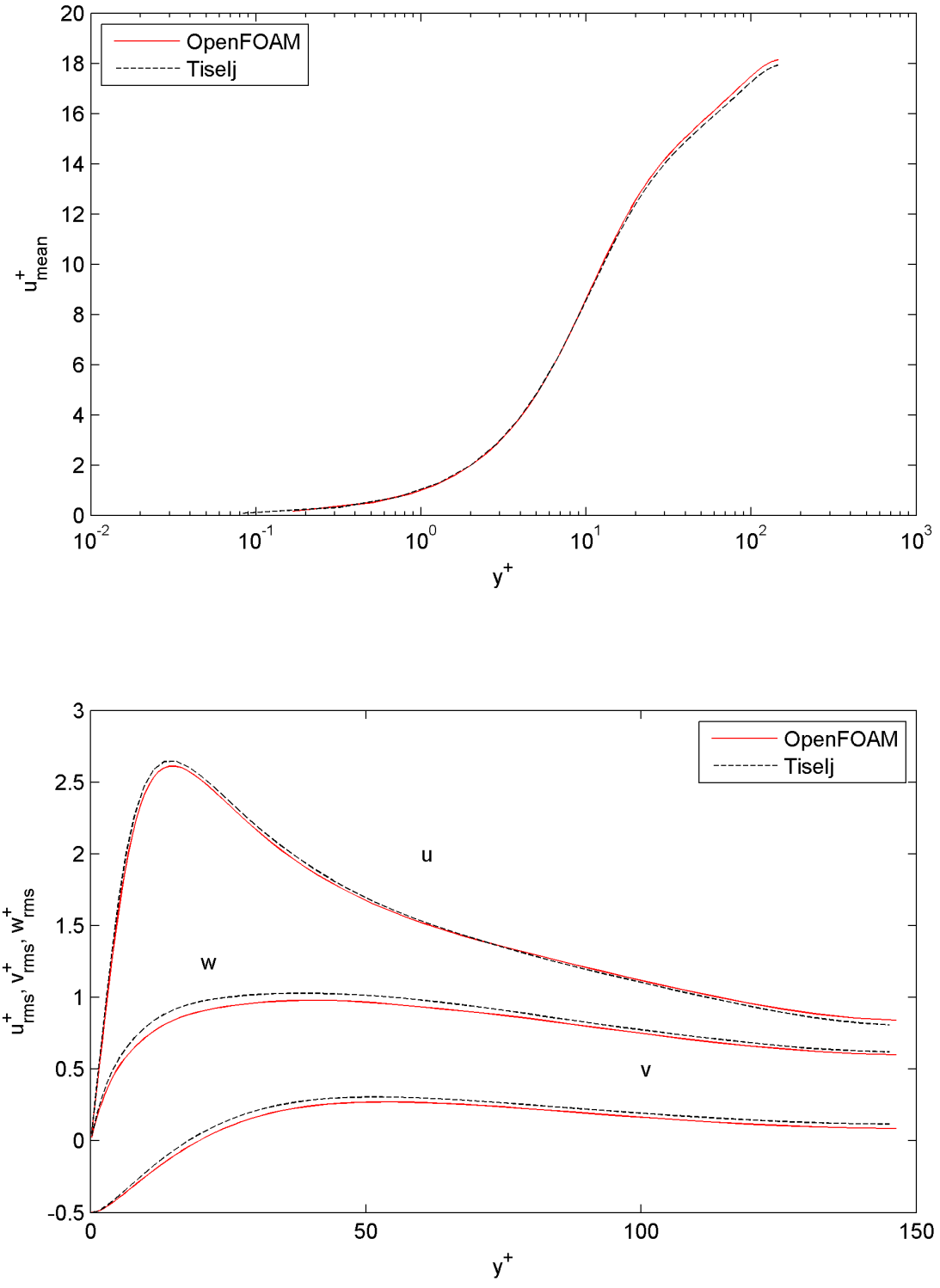

Figure 4.10.: Results for the velocities obtained with OpenFOAM. Results for the channel flow at $Re_\tau = 150$ are shown. Results for v^+_{rms} translated by -0.5 for visibility.

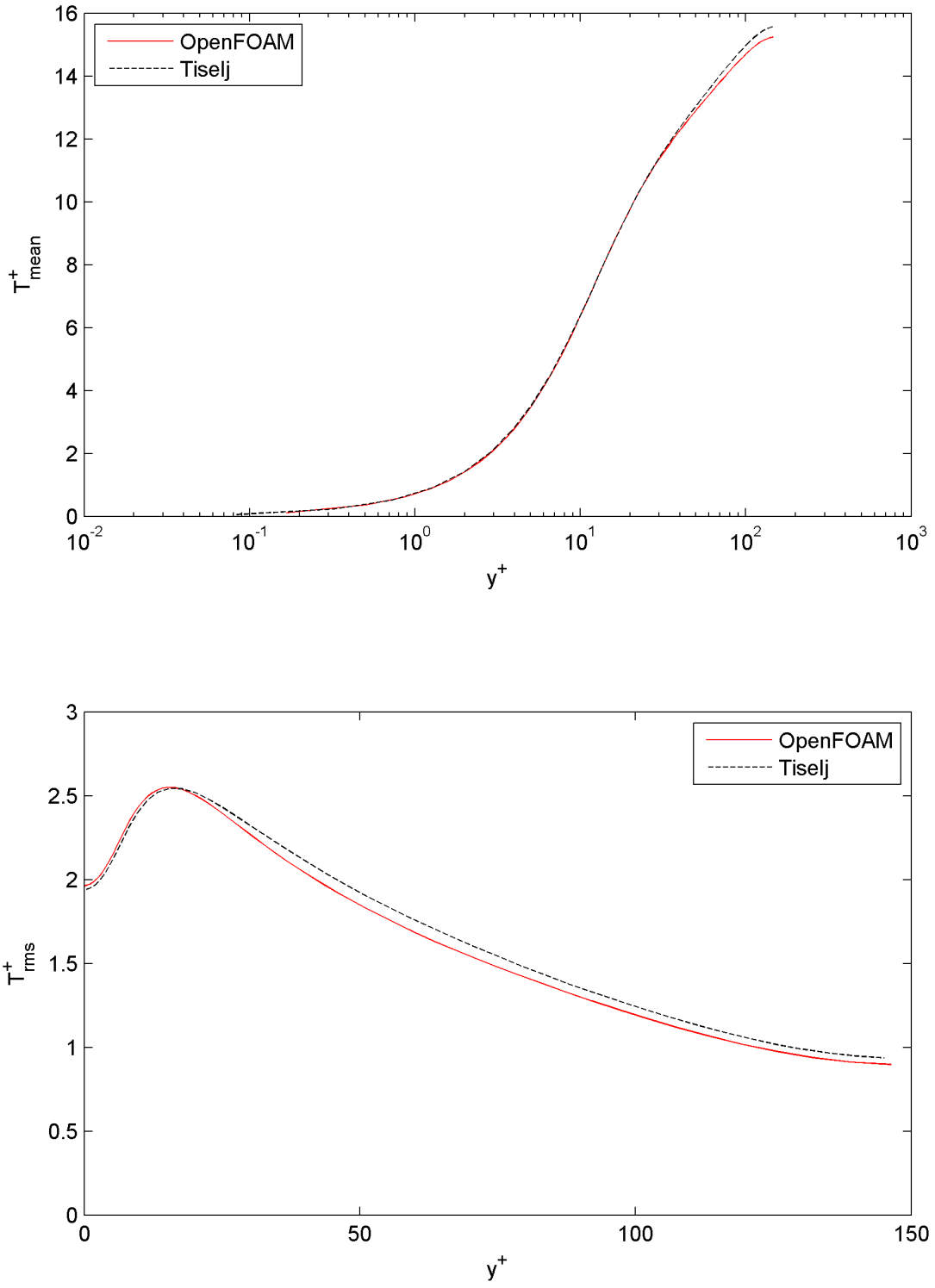

Figure 4.11.: Results for the conjugate heat transfer in the fluid, obtained with OpenFOAM. Results for the channel flow at $Re_\tau = 150$, $Pr = 0.71$, $K = 1$ and $d^{++} = 1$ are shown.

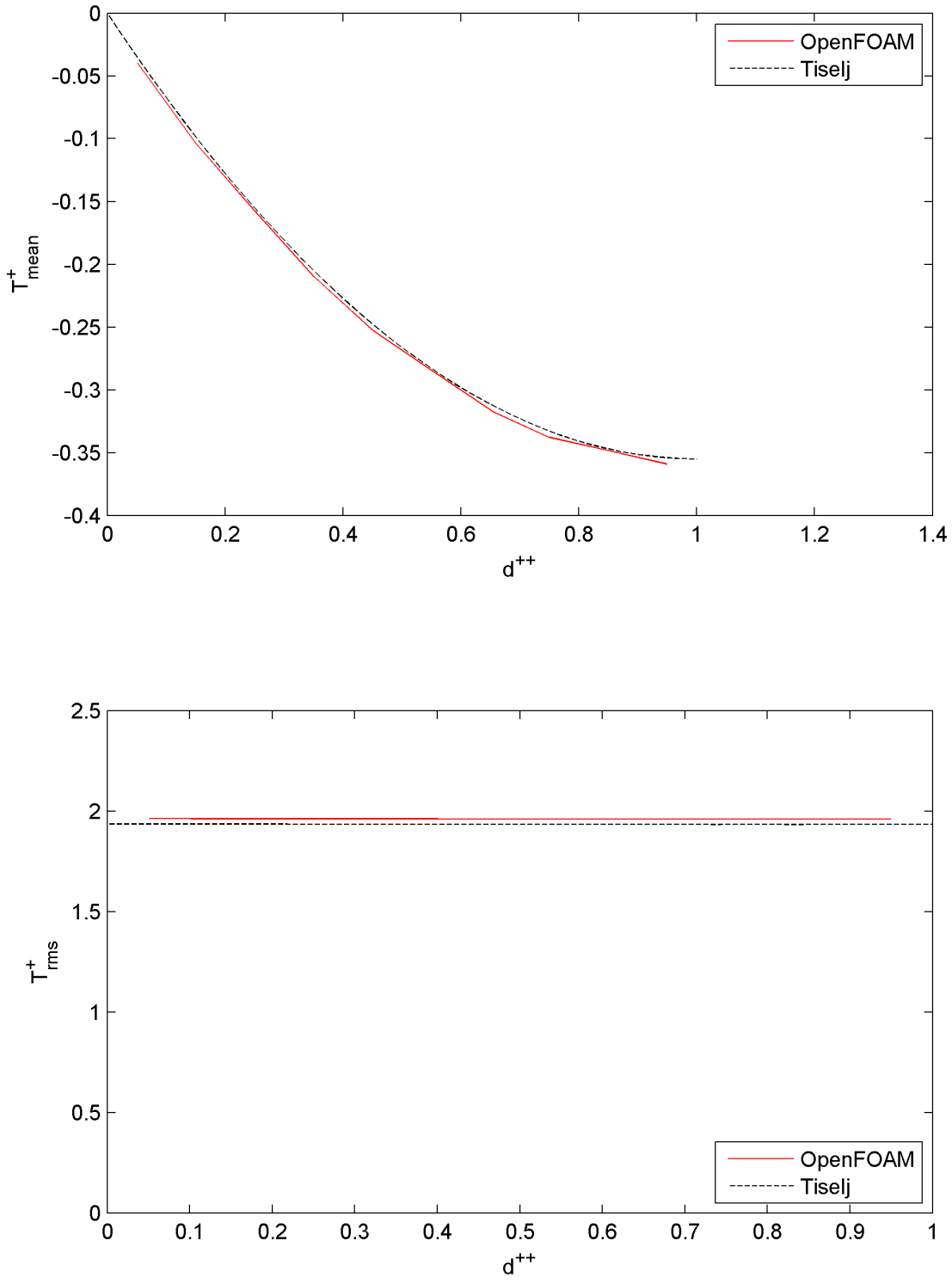

Figure 4.12.: Results for the conjugate heat transfer in the solid, obtained with OpenFOAM. Results for the channel flow at $Re_\tau = 150$, $Pr = 0.71$, $K = 1$ and $d^{++} = 1$ are shown.

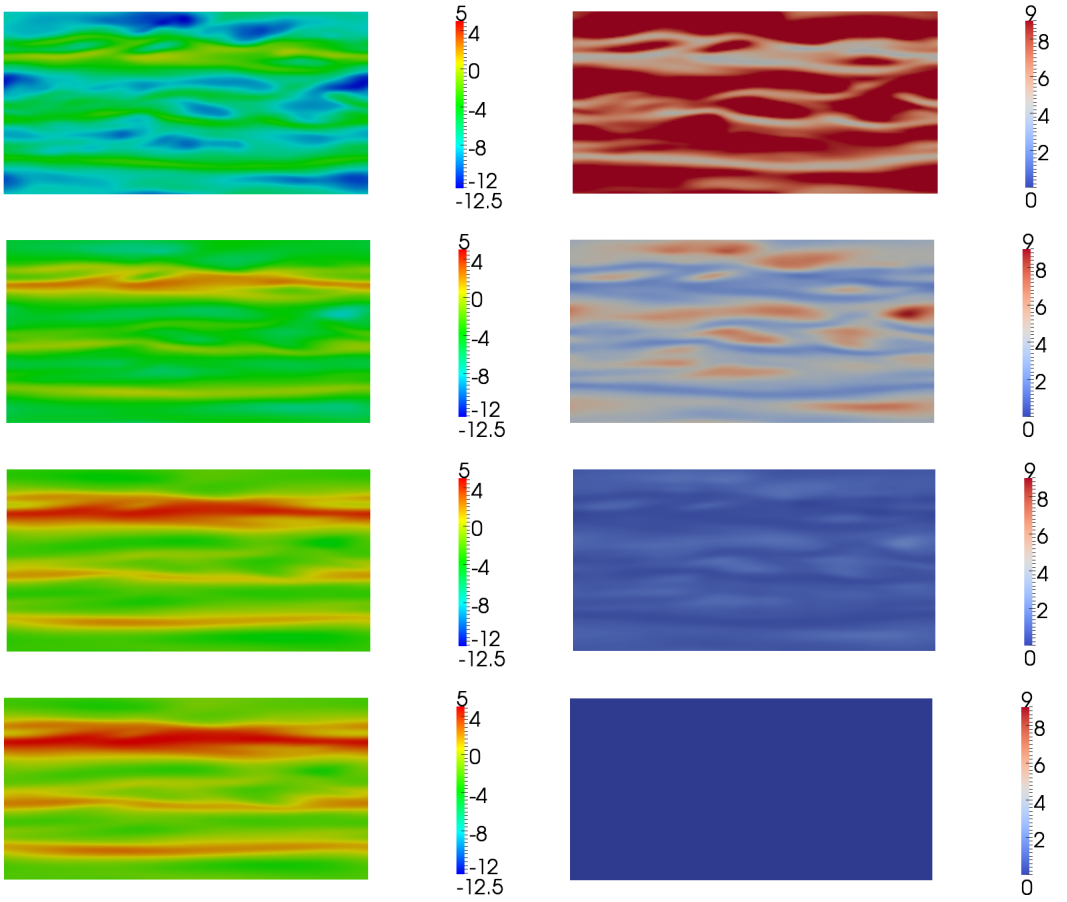

Figure 4.13.: Slices visualizing the results for the conjugate heat transfer simulation in a channel. On the left temperature is visualized, on the right velocity. As we go from top to bottom slices can be seen at $y^+ = 12$, $y^+ = 5$, $y^+ = 1$ and $y^+ = 0$.

4.6. DNS results for pipe flow

In this section results for the turbulent pipe flow will be presented. First results for the pipe flow meshed using extruded polyhydral cells will be presented in Section 4.6.1. Next, the results for the pipe flow meshed using full polyhydral cells will be presented in Section 4.6.2. Heat transfer is only simulated in the pipe meshed using extruded polyhydral cells, this is also presented in Section 4.6.1. Different CDS will be used in this section, for a description please read Appendix A.3.

4.6.1. DNS results for pipe flow using extruded polyhedral cells.

The properties of the simulation of the pipe flow, meshed with the extruded polyhydral mesh are presented in Table 4.5.

Results obtained with OpenFOAM can be seen in Figure 4.14. Results obtained with STAR-CCM+ can be seen in Figure 4.15. In these Figures results are shown in cylindri-

Table 4.5.: The computational details of the pipe flow simulated using extruded polyhydral cells. As can be seen in Figure 3.4 for such a mesh the cell size in the bulk varies from cell to cell. Therefore an estimate of the average cell diameter is given in this table.

Re_τ	180
Pr	1
number of cells	3.0 million
domain (z, r), (z^+, r^+)	6.4, 2 meters 1152, 360
mesh Δr^+, Δz^+, $\Delta\theta^+$	0.2-3.2, 6, 4.7
diameter poly in bulk	+/- 6 wall units
number of prism layers	55
prism layer thickness	0.35 meter, 63 wall units
SR	1.05

cal coordinates. Please keep in mind that calculations were performed using cartesian coordinates, and results transformed into cylindrical coordinates. Both codes perform good, STAR-CCM+ performs a bit better than OpenFOAM.

The results for the temperature can be seen in Figure 4.16. As can be seen three different convection differencing schemes were tested for the temperature, since instability issues were expected in the T-junction geometry, see Section 5. The error in Figure 4.16 in the center of the channel is quite large (around 20 %). However, as seen in Figure 4.5 the results obtained by Saad deviate strongly from the other two references in the center of the channel (y^+ 170). This explains the large difference that is found in the center of the channel comparing my results with Saad in Figure 4.16. The results for the three different CDS differ slighlty with respect to eachother.

4.6.2. DNS results for pipe flow using full polyhedral cells.

Table 4.6.: The computational details of the pipe flow simulated using full polyhydral cells in STAR-CCM+. As can be seen in Figure 3.4 for such a mesh the cell size in the bulk varies from cell to cell. Therefore an estimate of the average cell diameter is given in this table.

Re_τ	180
number of cells	3.7 million
domain (z, r), (z^+, r^+)	6.4, 2 meters 1152, 360
mesh Δr^+, Δz^+, $\Delta\theta^+$	0.2-3.2, 6, 4.7
diameter poly in bulk	+/- 6 wall units
number of prism layers	55
prism layer thickness	0.35 meter, 63 wall units
SR	1.05
CDS	bounded central

For the channel, and for the pipe flow using extruded polyhydral cells, the computational details were kept the same as much as possible between OpenFOAM and STAR-CCM+. This was not done for the simulations using the full polyhydral cells. As can be seen

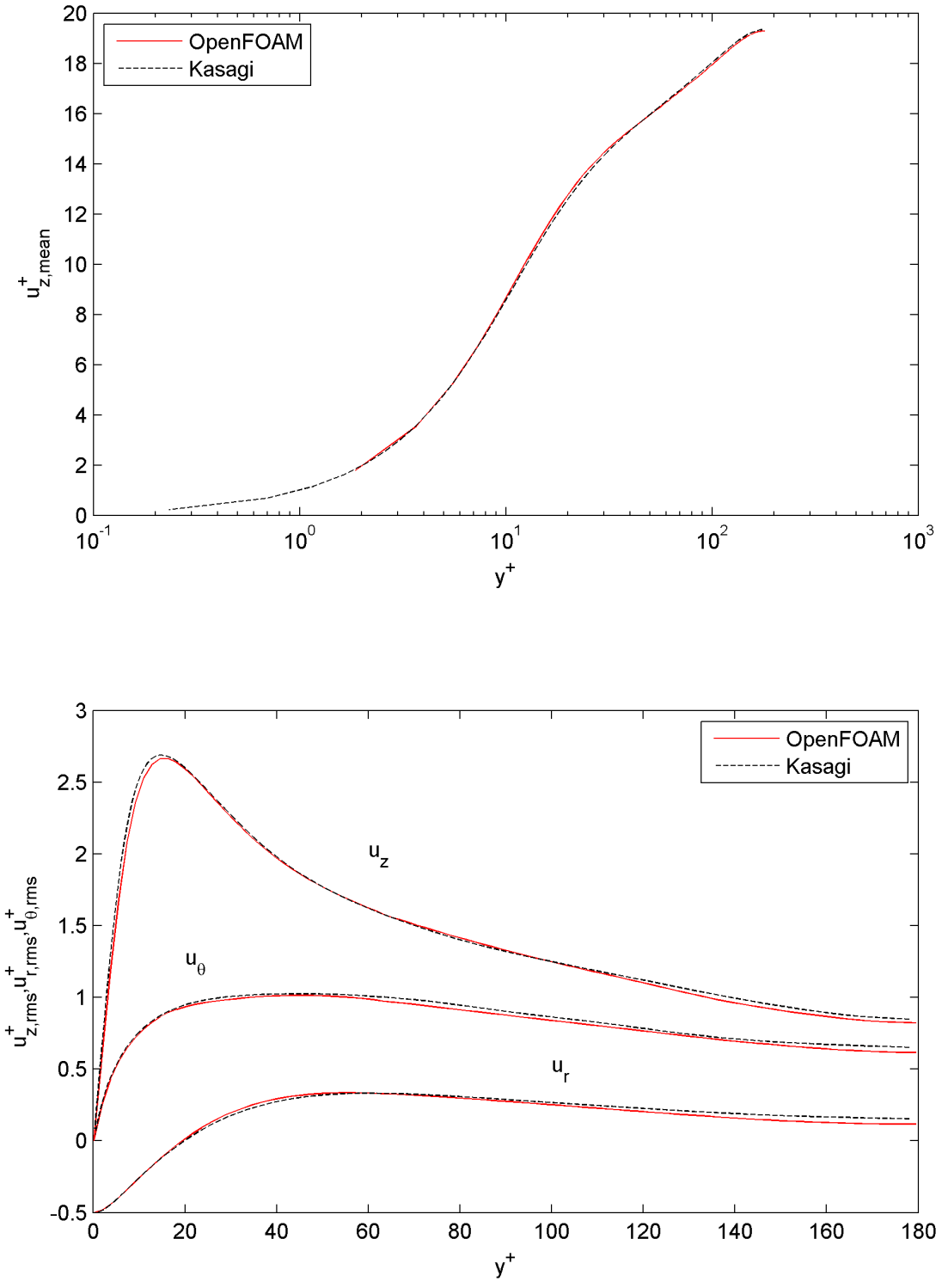

Figure 4.14.: Results for the pipe flow at $Re_\tau = 180$, meshed using extruded polyhydral cells. Results for $u^+_{r,rms}$ translated by -0.5 for visibility. Results obtained with OpenFOAM.

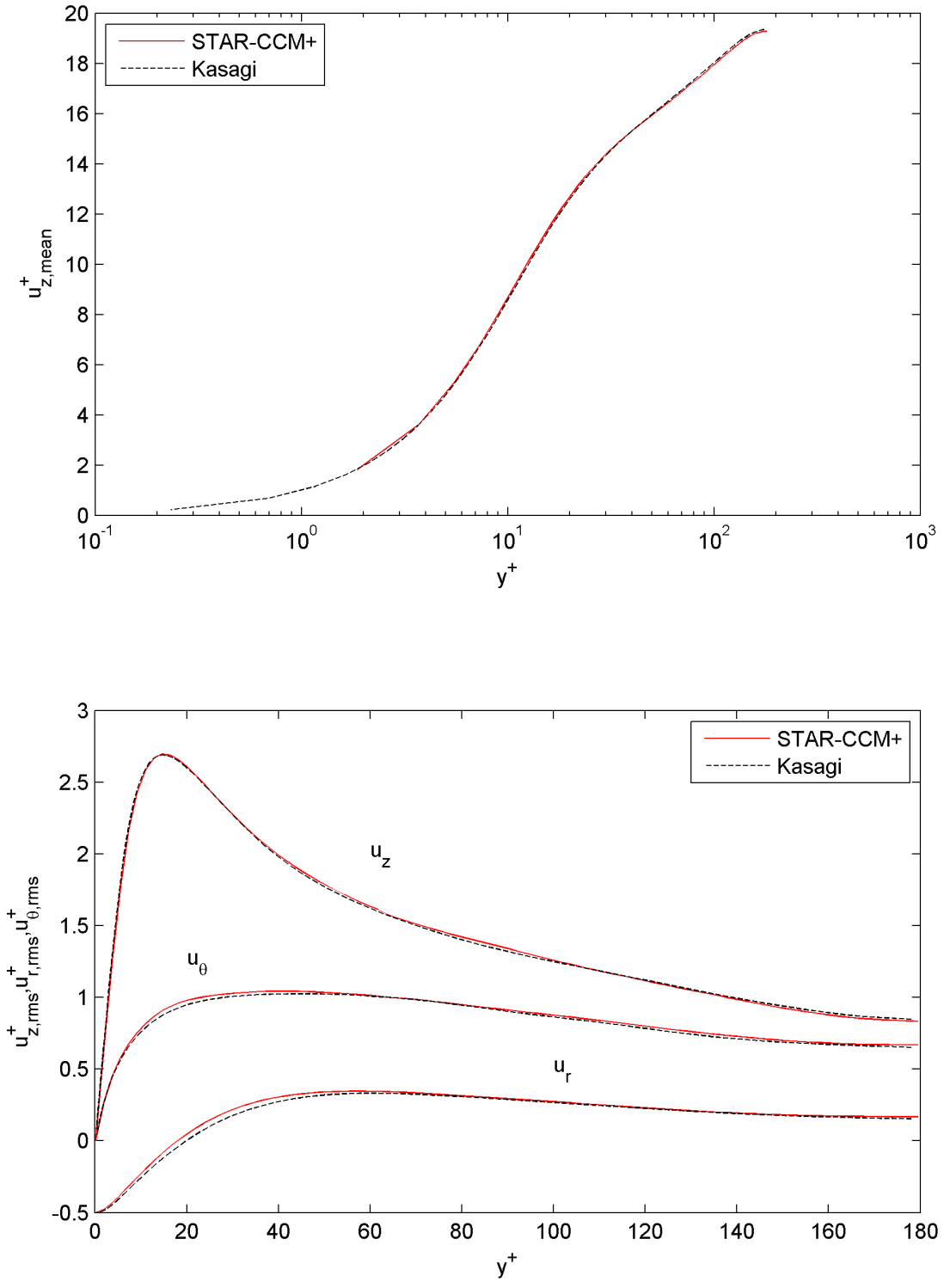

Figure 4.15.: Results for the pipe flow at $Re_\tau = 180$, meshed using extruded polyhydral cells. Results for $u^+_{r,rms}$ translated by -0.5 for visibility. Results obtained with STAR-CCM+.

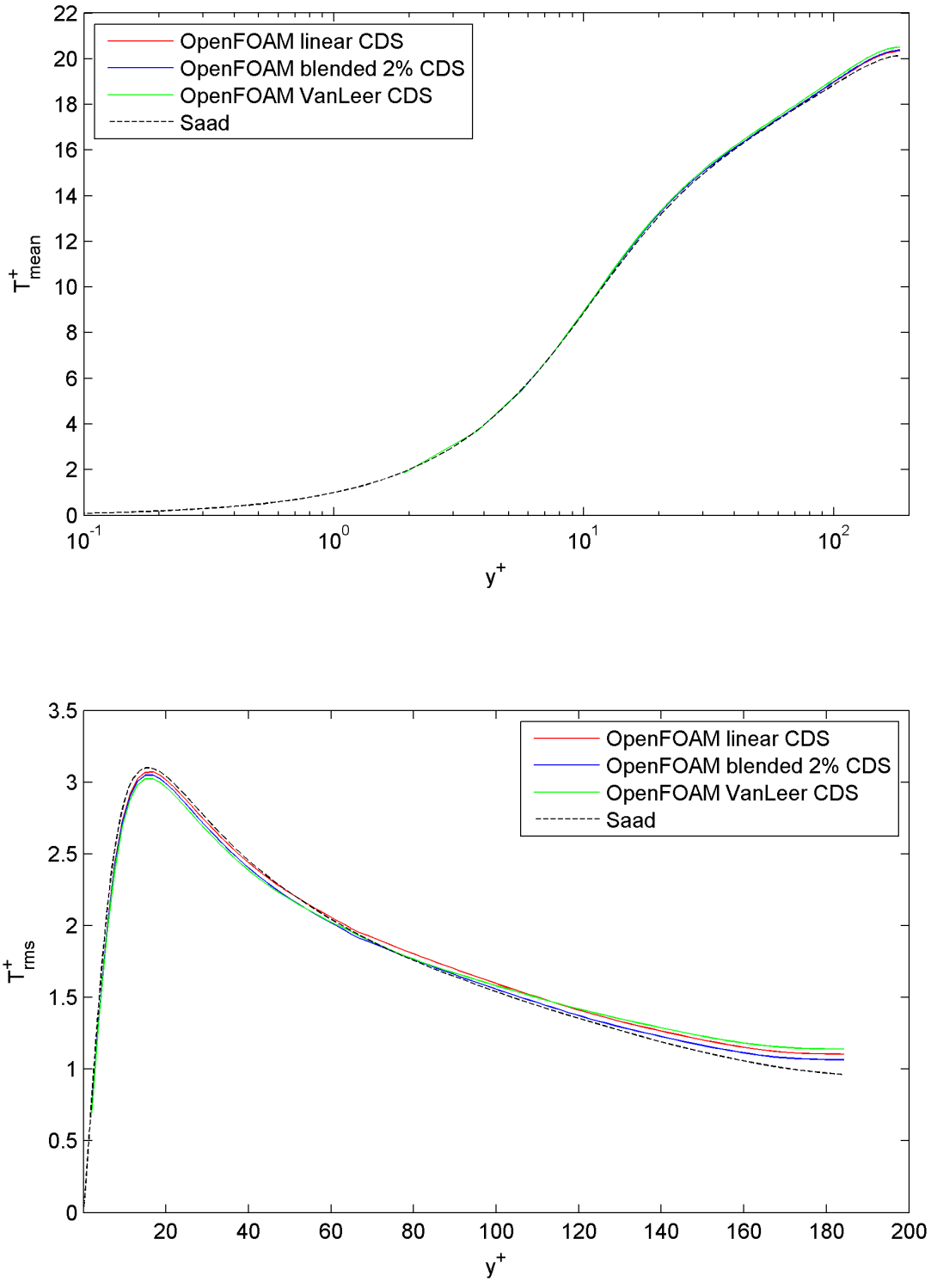

Figure 4.16.: Results for the temperature in the pipe flow at $Re_\tau = 180$ and $Pr = 1$, meshed using extruded polyhydral cells. Results obtained with OpenFOAM. Three different CDS are shown.

Table 4.7.: The computational details of the pipe flow simulated using full polyhydral cells in OpenFOAM. As can be seen in Figure 3.4 for such a mesh the cell size in the bulk varies from cell to cell. Therefore an rough approzimation of the average cell diameter is given in this table.

Re_τ	180
number of cells	3.0 million
domain (z, r), (z^+, r^+)	6.4, 2 meters 1152, 360
mesh Δr^+, Δz^+, $\Delta\theta^+$	0.5-2.3, 6, 4.7
diameter poly in bulk	+/- 6 wall units
number of prism layers	33
prism layer thickness	0.35 meter, 63 wall units
SR	1.05
CDS	clippedLinear 0.8 CDS

in Table 4.7 and Table 4.6 the mesh was not kept the same as well as the convection differencing scheme.

Star-CCM+ did not have any stability issues using this mesh in combination with the bounded central scheme, and results are good (see Figure 4.18). However, OpenFOAM had a lot of stability issues using the mesh that was used in STAR-CCM+. Trying to stabilize the simulation in OpenFOAM using a blended scheme or a limited scheme resulted in either instability or laminarization of the flow. It was observed that the stability issues in OpenFOAM originated from wiggles which appeared in cells that were highly stretched, thus in regions of the mesh were rapid variations in cell sizes were present. This can be explained by analyzing the kinetic energy conservation properties of a CDS, as demonstrated in appendix B. Using this knowledge it was chosen to reduce the number of cells that rapidly vary in size by decreasing the prism layer thickness. Furthermore the clippedLinear scheme was used which provides a good compromise between the accuracy of the linear scheme and the stability of the midPoint scheme. The clipping factor 0.8 was determined after some analysis of stability (thus using less clipping, for instance 0.7, gave instabilities).

4.7. Conclusions for the channel and pipe flows

The major question of this thesis, what kind of accuracy can be achieved with off-the-shelf software packages, such as OpenFOAM and STAR-CCM+, and using complex cell types, can be answered using the results in this chapter. The focus of the conclusion will be towards the peak in the u^+_{rms} and T^+_{rms} values. These peaks are generally most difficult to predict for the solvers. Furthermore the near wall behaviour is more important for accurately calculating the heat flux towards the wall than the accuracy obtained in the center of the channel.

For the channel flow the accuracy is satisfactory. Peaks in u^+_{rms} are within a few percent of the reference solution (see Figure 4.6). Results for the temperature are less good, differences between the T^+_{rms} peaks obtained and the reference solution are around 4 % for $Pr = 2$ (see Figure 4.7). However it must be said that the reference solution

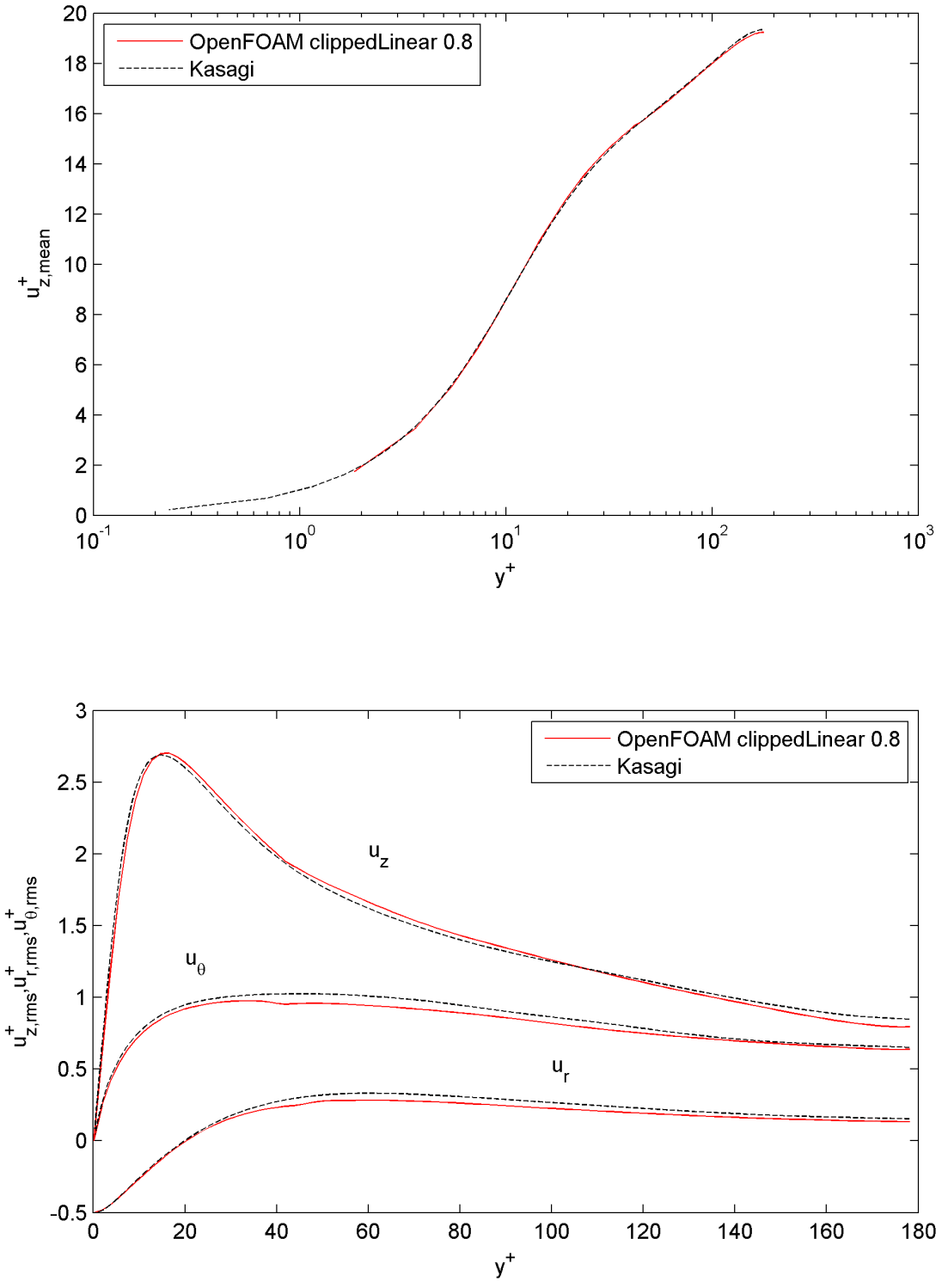

Figure 4.17.: Results for the pipe flow at $Re_\tau = 180$, meshed using full polyhydral cells. Results for $u^+_{r,rms}$ translated by -0.5 for visibility. Results obtained with OpenFOAM. The clippedLinear CDS is used.

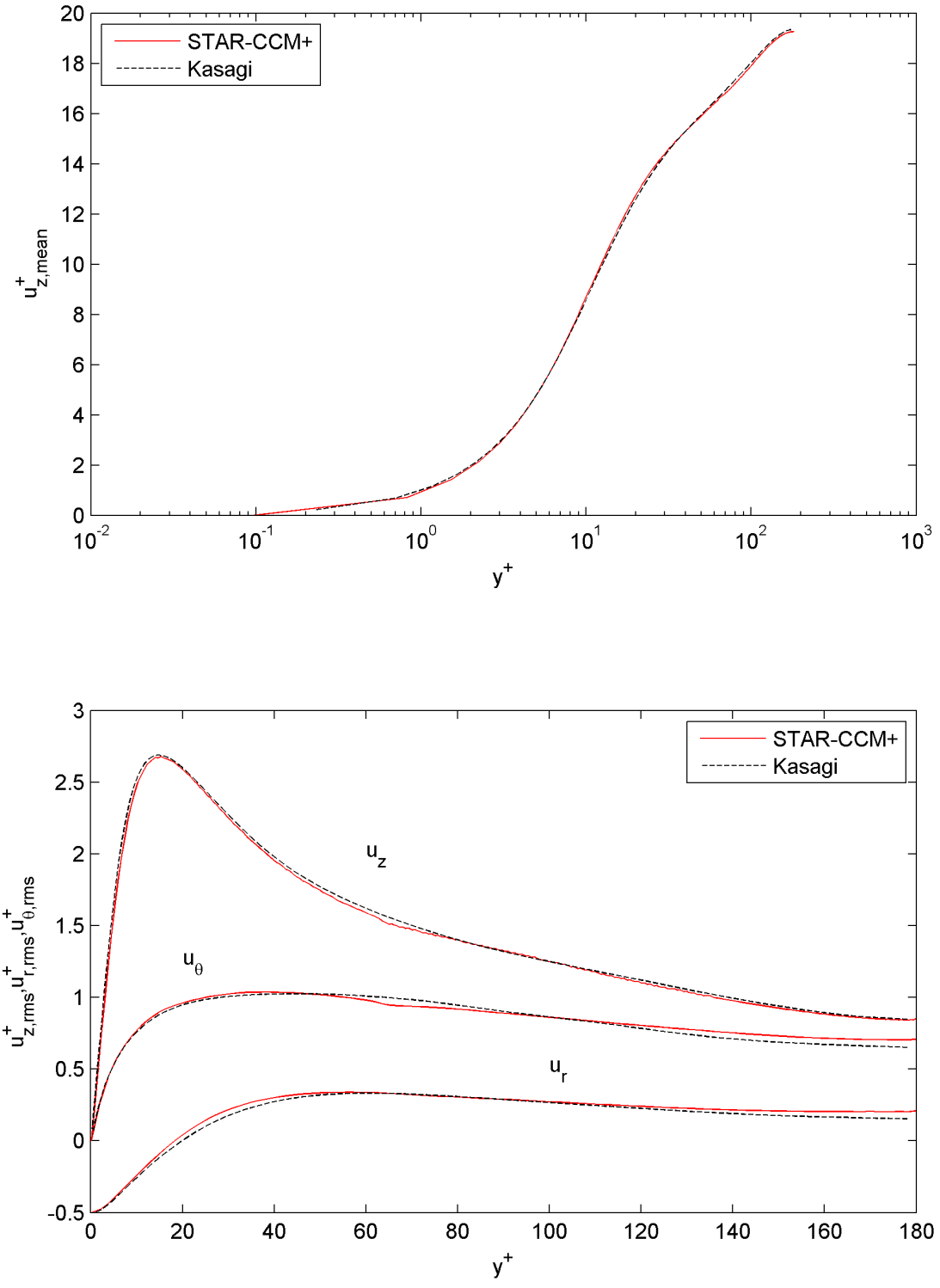

Figure 4.18.: Results for the pipe flow at $Re_\tau = 180$, meshed using full polyhydral cells. Results for $u^+_{r,rms}$ translated by -0.5 for visibility. Results obtained with STAR-CCM+. The bounded central CDS is used.

used in Figure 4.7 (the Kawamura reference with 250 million points, see Figure 4.3) displays the largest peak in u^+_{rms} and T^+_{rms} when compared to the other reference solutions. This reference was chosen since all three Prandtl numbers were available in this reference. Results obtained with STAR-CCM+ show comparable accuracy with respect to OpenFOAM (see Figures 4.6 and 4.8).

The simulation with conjugate heat transfer shows less accuracy than the simulation without conjugate heat transfer, when comparing the mean and root-mean-squares of the velocities (compare Figure 4.10 with Figure 4.6). As discussed when described the results this could be explained by the sice of the domain that was used for this thesis.

The flow in the extruded pipe is very accurate (see Figure 4.14 and 4.15), results are within a few percent of the reference solution.

The temperature in the extruded pipe is very accurate (see Figure 4.16) when looking at the peak in T_{rms}. The error in the center of the channel is quite large (around 20 %), this can agian be explained when analyzing the references.

For the full polyhydral cells the peaks are also captured very accurately (see Figure 4.17 and 4.18). However, the influence of the interface between the prism layer and the bulk region can clearly be seen. This can be seen around $y^+ = 40$ for OpenFOAM (see Figure 4.17) and around $y^+ = 63$ for STAR-CCM+ (see Figure 4.18).

Summarizing, it can be concluded that satisfactory accuracy can be achieved using both OpenFOAM and STAR-CCM+. On all three cell-types good accuracy can be achieved. Thus, the approach of using OpenFOAM or STAR-CCM+ for a DNS in a complex geometry using complex cell types is certainly valid.

5. Direct numerical simulation of a T-junction

This section will present results for the T-junction problem. Section 5.1 will introduce the problem and the flow regimes. Section 5.2 discusses the computational details, such as mesh and solver settings. Results will be presented in section 5.3.

5.1. Introduction to the T-junction problem

The geometry of the T-junction can be seen in figure 5.1. This geometry will also be used in the experiments performed within the Mother project, a research project funded by the EU concerned with the modelling of heat transfer in a T-junction geometry. The geometry of the T-junction is described in table 5.1.

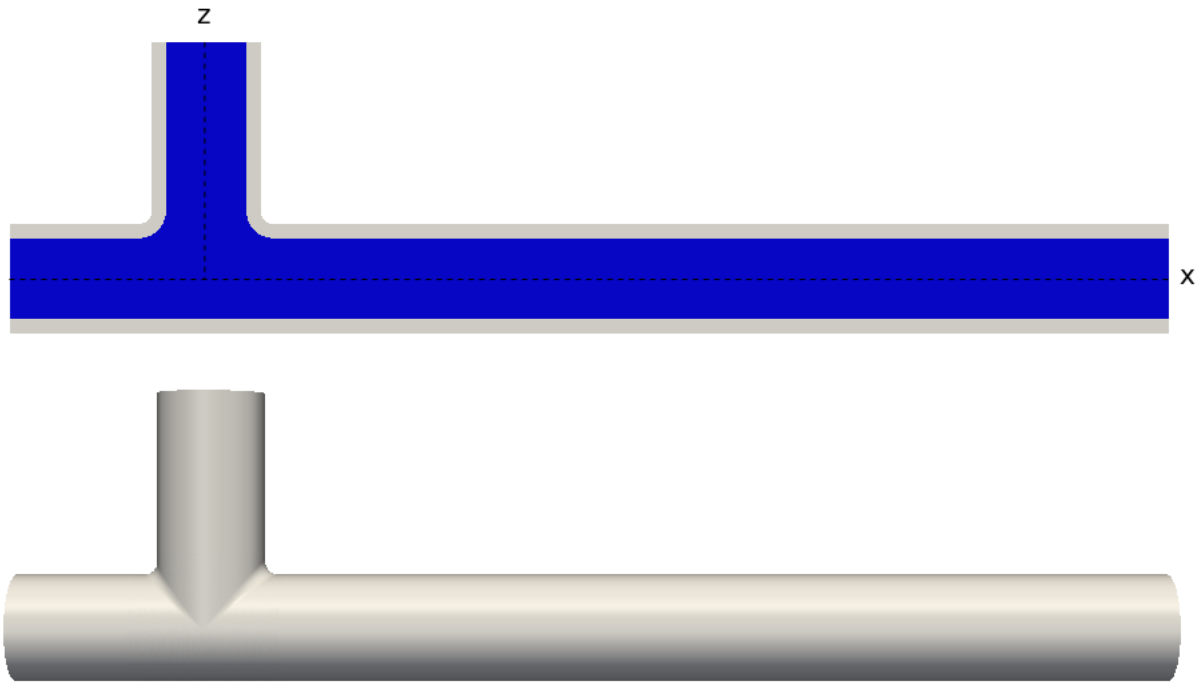

Figure 5.1.: The T-junction geometry. On top a section of the T-junction can be seen where the fluid has been coloured blue and the solid grey. On the bottom the outside of the T-junction can be seen.

Table 5.1.: Properties of the geometry of the T-junction. Lengths of pipe measured from the origin. The origin is located at the intersection of axis of the intersecting pipes (as seen in Figure 5.1).

diameter	54 mm
radius of internal bend	18 mm
wall thickness	9.54 mm
length outlet pipe	12 diam.
length inlet pipe top	3 diam.
length inlet pipe front	2.5 diam

The flow regime is defined as follows. The Reynolds number used to define the flow regime is the bulk Reynolds number based on the bulk velocity in axial direction (u_{bulk}) and the pipe diameter (δ):

$$Re_b = \frac{u_{bulk}\delta}{\nu} \tag{5.1.1}$$

The two inflow pipes are set to have a fixed inlet profile. The inlet profile is the parabolic laminar profile (this can be seen in Figure 5.2), corresponding to Reynolds number $Re_b = 2188$. This will results in a Reynolds number of $Re_b = 4376$ in the outlet pipe. The inflow Reynolds numbers are tuned to generate this outflow Reynolds number. The outflow Reynolds number was chosen to be equal to a pipe flow simulation, where the Reynolds number based on the friction velocity was $Re_\tau = 150$. The boundary condition for the wall was no-slip. For the outlet a fixed pressure boundary condition was used.

The Prandtl number was set to $Pr = 1$. The inflow in the top pipe was set to a temperature of 1 and at the left pipe to a temperature of 0 (see Figure 5.2). For the temperature, three different boundary conditions for the wall were used. The adiabatic wall simulating no heat flux across the wall, the fixed temperature wall simulating no change in temperature of the solid and conjugate heat transfer. For the fixed temperature boundary condition the temperature was set to 0.5. For the conjugate heat transfer simulation the activity ratio was set to 1. This combination of parameters gives a non-dimensional thickness for the pipe wall of $d^{++} = 12$. The flow regime is visualized in Figure 5.2.

5.2. Computational details

The mesh for the fluid was based on the experience obtained during the direct numerical simulations of the pipe flow. The T-junction was meshed using a combination of full polyhedral cells and extruded polyhedral cells. The solver setting was kept the same as much as possible for the pipe flows. The computational details for pipe flow using extruded polyhydral cells can be seen in Table 4.5, the computational details for pipe flow using full polyhydral cells can be seen in Table 4.7. The computational details for the T-junction will be descriped in the following paragraphs.

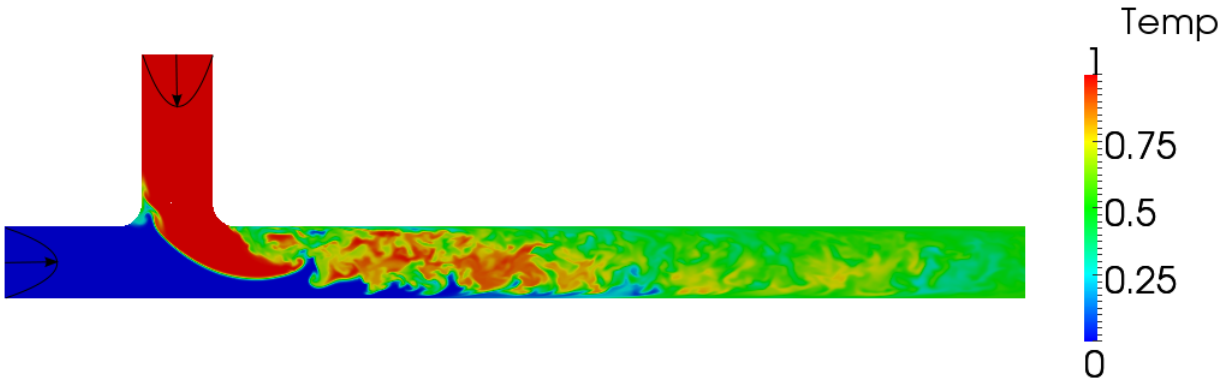

Figure 5.2.: The flow regime for the T-junction. The parabolic inflow profiles can be seen as well as the inflow temperatures. The sharp interface between the hot (red) and cold (blue) flows can clearly be seen.

First, it must be realized that the concept of wall units is less clearly defined for a complex geometry than for instance for a channel or pipe flow. The averaged (in time) wall friction has the same value everywhere in a channel or pipe flow. For a complex geometry this is certainly not the case. So how is a general wall unit defined which can be used for meshing? For the T-junction the choice was made to use the wall unit obtained in a pipe flow at $Re_\tau = 180$. A mesh was constructed based on this value. In figure 5.3 the mesh in the T-section of the T-junction can be seen. The T-section of the T-junction is the location where the two pipes meet. The prism layers used is 0.012m thick, the stretching ratio used is 1.05 and the number of prism layers is 33. The total number of cells used was 22 million, 14 million for the fluid region and 8 million for the solid region.

To get a rough idea for the flow and to check for areas of locally high friction a preliminary RANS calculation was performed using STAR-CCM+. The RANS model used is the non-linear k-epsilon model [32]. The results obtained during this simulation can be seen in figure 5.4.

For the mesh of the solid the surface mesh of the fluid was simply extruded in wall-normal direction. The number of cell layers used was 30 using equidistant spacing. This number of cell layers was based on the mesh guidelines provided by [33].

For the discretization choices had to be made for the convection differencing scheme, both for the momentum equation and the energy equation. The CDS for the momentum equation was set to the clippedLinear scheme for the full polyhydral mesh, and the linear scheme was chosen in the extruded polyhydral mesh. In OpenFOAM it is possible to use different schemes on different locations in the domain. This choice was rather straightforward since the clippedLinear scheme produced fairly accurate results during the simulation of the pipe flow using a full polyhydral mesh and was also stable. The linear scheme was used in the extruded polyhydral mesh since it ran stable and is the most accurate scheme available in OpenFOAM.

The choice of the convection differencing scheme for the energy equation was less straightforward. Based on the simulation in the pipe it seems tempting to use the same combination of schemes as for the momentum equation (clippedLinear i.c.w. linear).

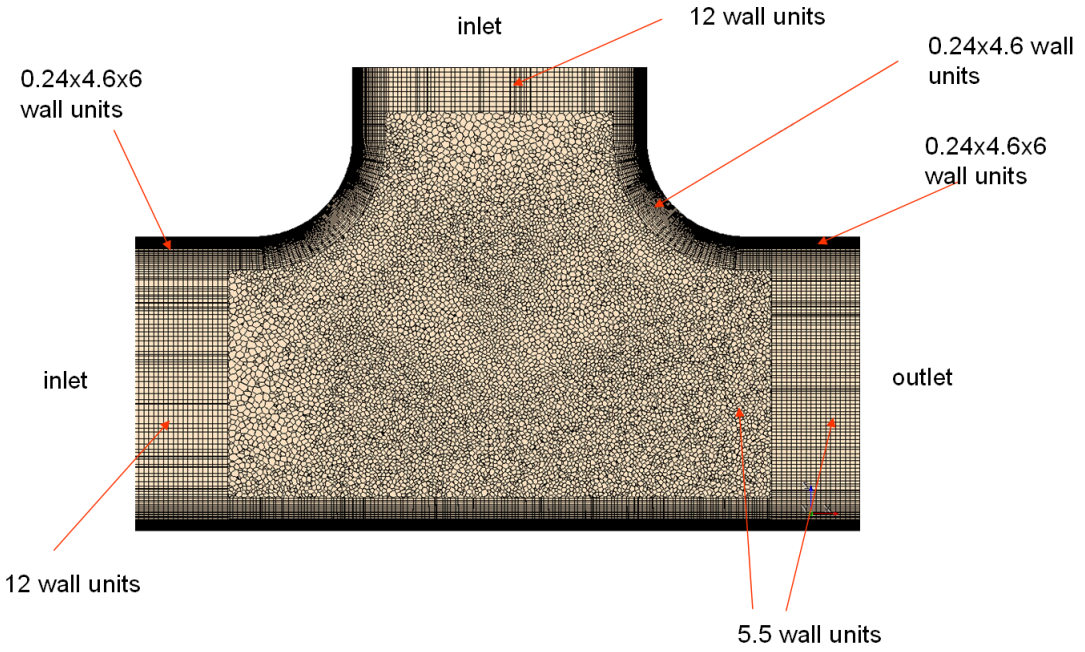

Figure 5.3.: The mesh of the T-junction, only the mesh for the fluid part is shown. It can clearly be seen that the actual T-section is meshed using full polyhydral cells. The sections of pipe which are straight are meshed using extruded polyhydral cells. Arrows pointing to the middle region of the pipe's denote roughly the diameter of the cells in that region. Arrows pointing to the prism layer region (at the walls) denote the cell size at the wall. Cell sizes at the wall are given as wall-normal direction and diameter for the full polyhydral cell prism layer, or wall-normal, tangential and axial direction for the extruded polyhydral cell prism layer.

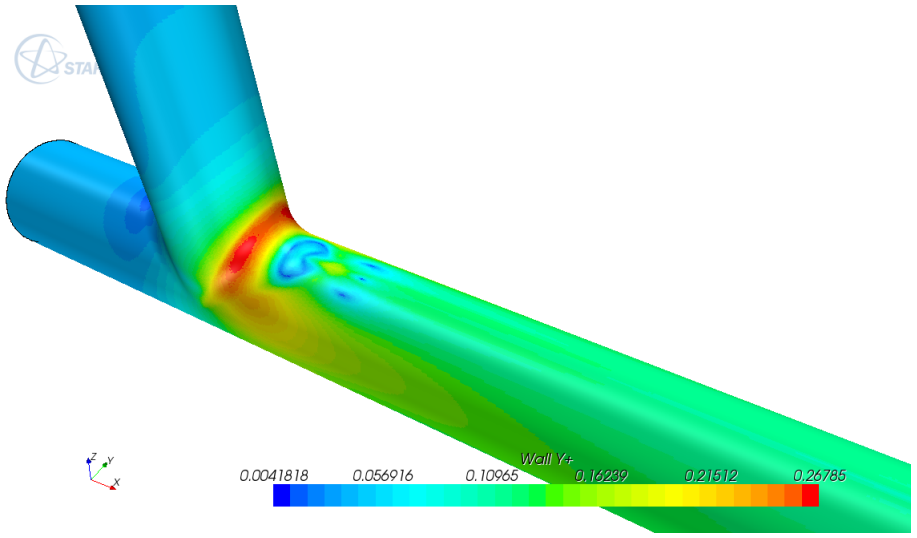

Figure 5.4.: Wall friction obtained using a RANS simulation. y^+ values are shown for the cell centers. According to the experience in the pipe these values should be $y^+ = 0.1$ in the extruded mesh and $y^+ = 0.25$ in the full polyhedral mesh.

However, due to the sharp gradient present in the T-junction between the hot and cold flow this produced instabilities (this sharp gradient can clearly be seen in Figure 5.2). Therefore the vanLeer scheme was chosen for the entire domain. This is not ideal, as will be discussed in Section 6.

5.3. Results for the T-junction simulation

First of all it must be said that this is a demonstration case. The mesh was created with great care and the solver settings likewise. However, the high cost of performing this simulation did not permit for sufficient flow through times. Roughly five flow-through times were used to perform averaging, in general it is advised to use at least ten flow-through times for these simulations [31]. This can also be observed in the results, since the averaged results should be symmetric in the xz plane. As can be seen in Figures 5.7 and 5.8, this is not the case. Therefore these results can not be considered to be statistically converged. However, a general analysis of flow behaviour is possible using this simulation.

First, the general flow dynamics will be described. As can be seen in Figure 5.5 several interesting dynamics are present. In the center of Figure 5.5 it can be seen that the cold flow (blue) is pushed downwards in the center of the T-junction directly after the actual T-section. This is combined with an upward flow at the sides of the T-junction, as can be seen in the slices at the bottom of Figure 5.5. This results in a flow where the hot streams is essentially captured inside the cold stream for a few diameters downstream of the T-section. During the first few diameters the hot stream is only able to heat the solid wall at the top of the T-junction, as can be seen at the top of Figure 5.5. The enclosure of the hot fluid by the cold fluid can also be seen in Figure 5.7 in the mean temperature field. As can be seen in Figure 5.8 the largest fluctuations in the temperature occur at the interface between the hot and the cold fluid.

Intermittent behaviour in the temperature can be seen in the slices in Figure 5.6. At 1.75 diameters downstream the slice hardly contains hot fluid as compared to 1.5 diameters downstream and 2.5 diameters downstream. This intermittent behaviour is created by the vortex shedding from the stagnation point on the left rounded corner of the T-junction. In Figure 5.5 formation of this vortex can be seen at the stagnation point, and a break-up of one of the shedded vortices can be seen at the end of the hot fluid (red) tongue extending from the T-section to the left.

Flow structures, which are similar to the flow structures in the channel (see Figure 4.13), can be seen in Figure 5.9. On the top of Figure 5.9 the thermal structures can be seen. A hot flow region can be seen extending from the boundary layer to the wall. The cold region directly past the T-section can be seen to correspond to the seperation bubble in the flow.

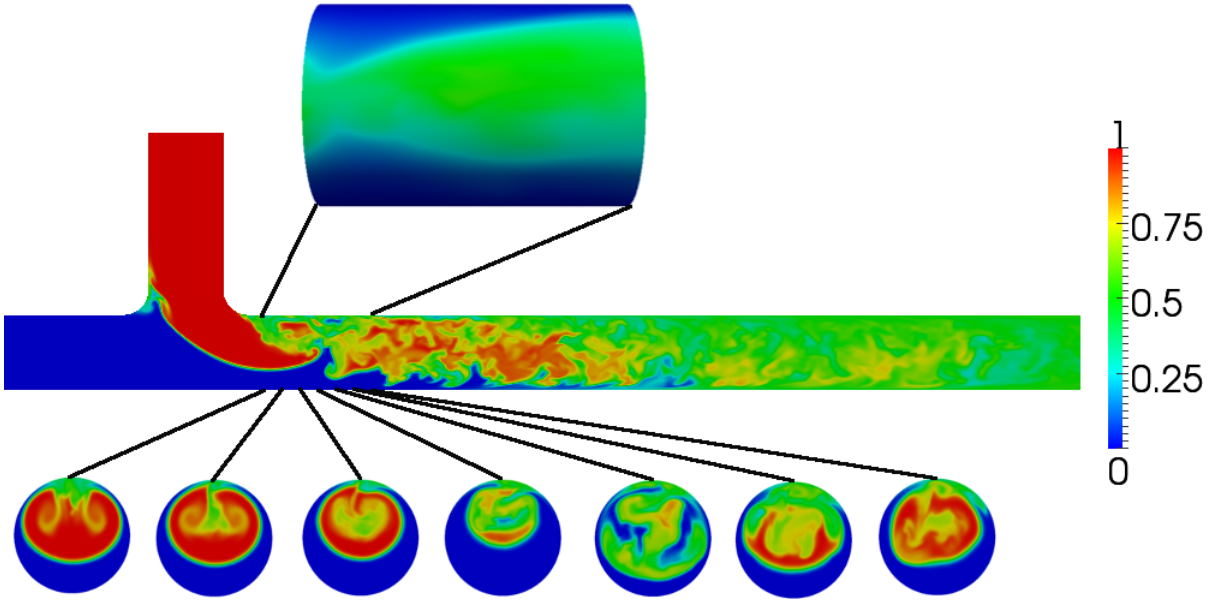

Figure 5.5.: Instantaneous temperature temperature structures. In the middle temperature in a slice can be seen, viewed from the side. On top the temperature on the interface between the solid and the fluid can be seen, viewed from the top. Slices on the bottom show the instantaneous temperature on different locations looking in axial direction.

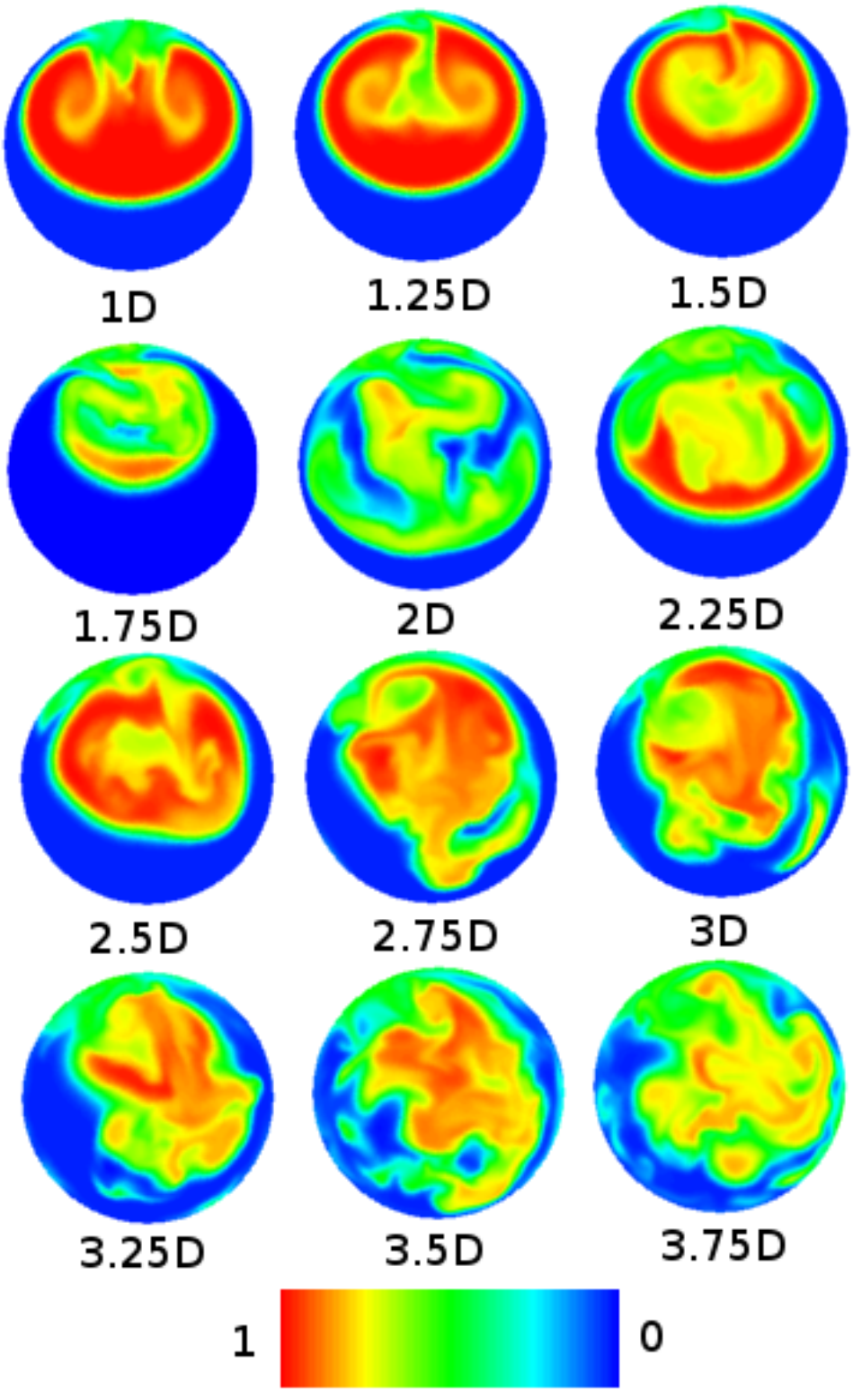

Figure 5.6.: Slices of the T-junction at different locations downstream of the origin. Instantaneous temperature shown.

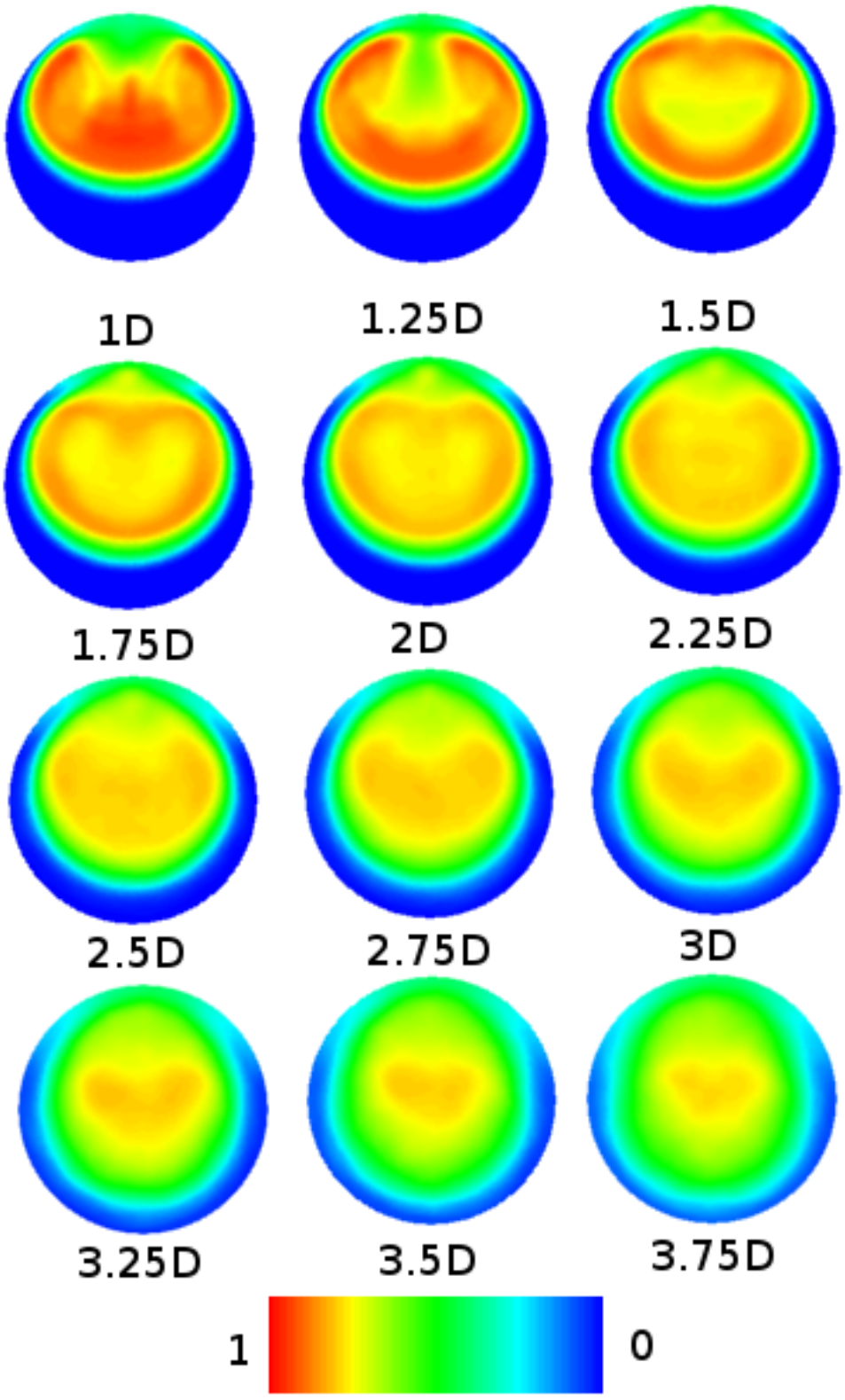

Figure 5.7.: Slices of the T-junction at different locations downstream of the origin. Mean temperature shown.

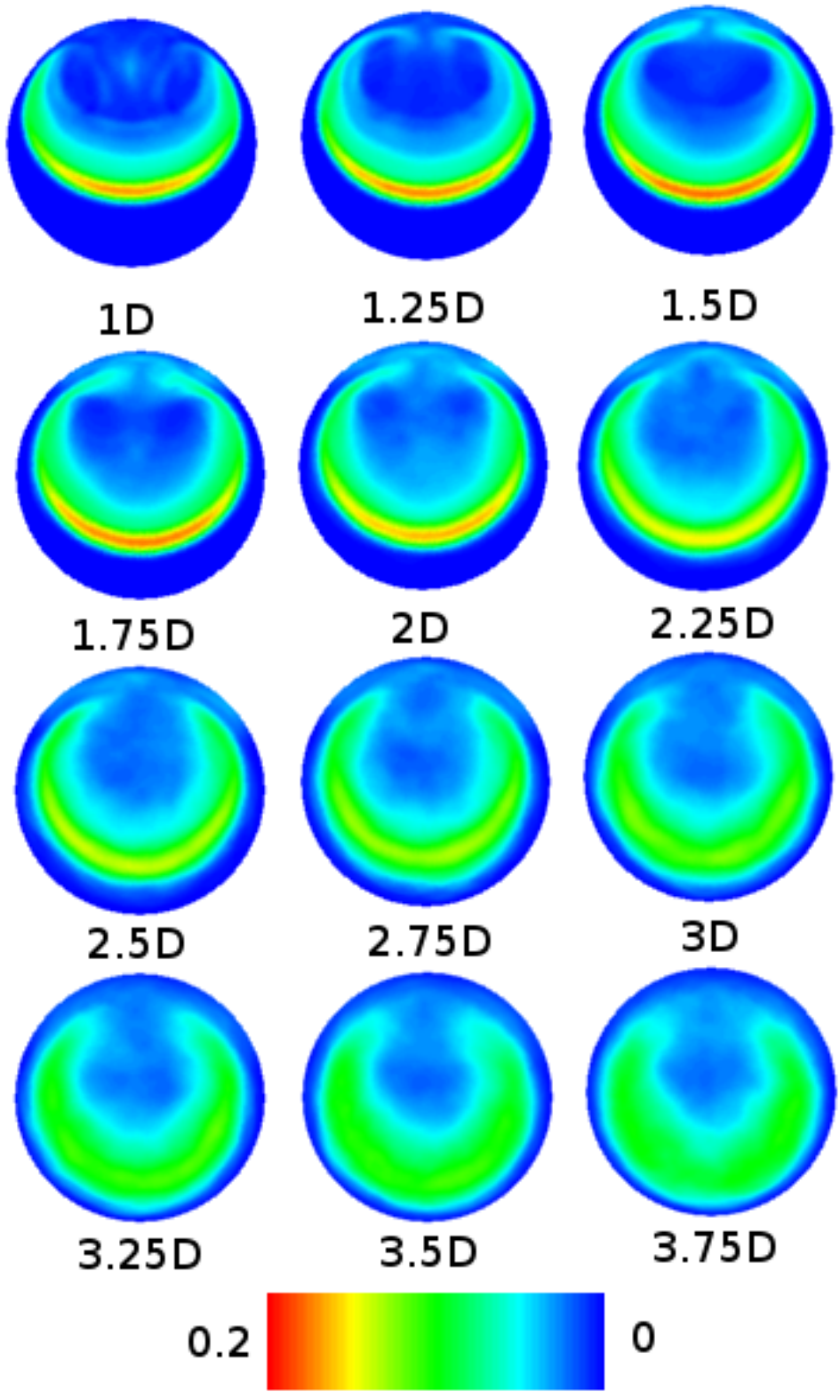

Figure 5.8.: Slices of the T-junction at different locations downstream of the origin. RMS of the temperature shown.

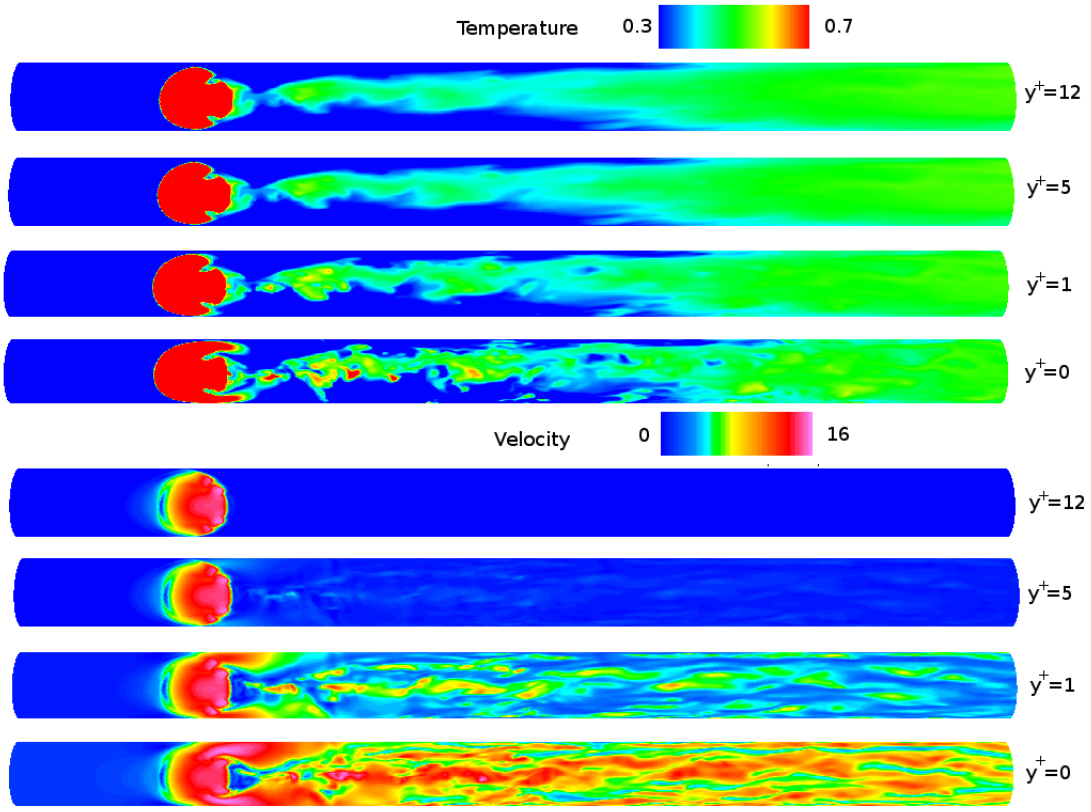

Figure 5.9.: Curved surfaces at different distance from the wall shown. On top the instantaneous temperature (clipped for visibility) can be seen. On the bottom the magnitude of the velocity vector can be seen.

6. Discussion, recommendations and conclusions

This chapter discusses the results of the thesis. In Section 6.1 some points concerning this work, based on this discussed some recommendations will be formulated. This chapter will be concluded in Section 6.2 with the general conclusions based on this thesis.

6.1. Discussion and recommendations

This section doubts the results in the spirit of Bertrand Russel. As said in the introduction there are no references for the T-junction simulation, so doubt must be used for analyzing the T-junction simulation.

6.1.1. What about the vanLeer CDS for the temperature equation?

The discretization of the convection term in the energy equation could be investigated further. The vanLeer convection differencing scheme was chosen for the T-junction simulation, since it performed reasonable in the turbulent pipe flow and was able to suppres instabilities in the T-junction. These instabilities originated from the sharp step profile in the beginning of the mixing process when the flow is essentially still laminar. However, such a step profile is not present in the turbulent pipe flow, neither are the fluid packets of hot (or cold) fluid travelling through the domain, which are present in the T-junction. These packets will create sharp gradients in the temperature field.

Since it is known that the vanLeer scheme will be more diffusive in the presence of sharp gradients, it can be expected that the accuracy of the scheme is decreased in the T-junction.

The accuracy of this scheme under these conditions could be investigated for instance by simulating the release of a passive scalar in a turbulent pipe flow [4]. It is interesting to see that in this reference also a TVD scheme was used for the discretization of the temperature equation. A TVD scheme is also used in the DNS of a T-junction performed by Fukushima [15]. A-posteriori, it could be calculated how much blending is introduced by the vanLeer scheme. This would give more confidence in the results, if it would turn out that the average amount of blending is low, or it could raise more

concerns if the average amount of blending turns out to be high. It is recommended that such an analysis is performed for the T-junction simulation.

6.1.2. What about higher/lower Prandtl numbers?

The case of a higher Prandtl number is interesting for the thermal fatigue analysis, since this often involves water. Even if the Prandtl number is allowed to vary with temperature during a simulation, the Prandtl number will be relatively high in regions where the fluid temperature is close to room temperature ($Pr \sim 7$). As we have seen in chapter 2 this will give Batchelor length scales smaller than the Kolmogorov length scale, further increasing the mesh-requirements for the simulation. However, as shown by Na and Hanratty [25] the requirement of the Batchelor scale could be too strict for practical purposes. Na and Hanratty essentially only refine in the wall-normal direction, when increasing the Prandtl number. The same is concluded by Bergant [3].

Futhermore, doing a simulation at a Prandtl number for water, would ease the comparison with experiments if experiments were to be performed using water. This is discussed within the Mother project.

6.1.3. What about the assumptions used to derive the equations?

As seen in section 3.1 quite a few assumptions were made in deriving the equations, which were used in the simulations performed in this thesis. These assumptions are repeated below:

- incompressible flow (ρ = constant)
- newtonian fluid
- no gravity
- constant thermal properties (α = constant and ν = constant)
- no dissipation source in the energy equation

First the assumptions of incompressible flow and no gravity will be discussed together. Next, the assumption of constant thermal properties is discussed.

Incompressible flow, no gravity
These assumptions are discussed together since their influence is the same. If one considers an actual thermal fatigue problem it often involves water. This if often considered to be higly incompressible, and to have constant density. However, it must not be forgotten that in the mixing process in a T-section, two flows are mixed with different temperatures. Since this temperature difference can be large, density differences in the order of a few percent can occur between the two mixing flows. This can lead to buoyancy effects often not recognized in literature (except in [7]) for mixing in a T-junction.

Table 6.1.: The variations of some properties of water with temperature.

T (^0C)	10	90
ν ($mPa \cdot s$)	1.307	0.315
k ($W/m \cdot K$)	0.584	0.676
c_p (kJ/kgK)	4.193	4.208
Pr	9.4	2.0

The influence of buoyancy is described in [15] for a simplified T-junction geometry and in [14] for a mixing layer with density differences. Both these reference show great influence of buoyancy on the turbulent mixing process. This is also to be expected in the T-junction.

The importance of buoyancy can be analyzed using two non-dimensional numbers. The importance of natural convection versus forced convection is determined by the ratio of the Grashof and Reynolds number. The Grashof number is given by [36]:

$$Gr = \frac{g\beta\Delta T L^3}{\nu^2} \tag{6.1.1}$$

The importance of buoyancy can be determined from this [36]:

- $Gr << Re^2$ forced convection dominates
- $Gr >> Re^2$ natural convection dominates

The neglegibility of buoyancy thus varies strongly from case to case. It was shown that the buoyancy effects were not negligeble in the failing of the Civaux PPN unit 1 in 1998 [7]. So, why this long discussion concerning buoyancy? In this thesis the flow in a T-junction was analyzed for its general behaviour. It must be realized that the general flow dynamics could look very different under the influence of buoyancy.

Constant thermal properties
The variation of the physical properties is strongly dependent on the fluid and the temperature ranges and operating pressures. To put things into perspective, the variation of physical properties for water at atmospheric pressure is given in table 6.1. It can clearly be seen that the assumption of constant thermal properties is not valid for the flow in an actual T-junction where temperature ranges will be even larger than in table 6.1.

6.1.4. Can we extrapolate obtained accuracy from a channel/pipe to a T-junction?

This is perhaps the must difficult and vital question up for discussion. The results in chapter 4 give confidence in the results, when a pipe or channel flow is simulated. But should we be as confident when simulating a complex geometry such as a T-junction? In other words, can we expect to obtain the same error margin in a T-junction? This is

a difficult question. If the flow is considered it can be seen that more flow dynamics are present in a T-junction than in a channel or pipe flow. Such as transition from laminar to turbulent flow and seperation. For the temperature equation more numerical diffusion can be expected as discussed in section 6.1.1 and it is well known that this will lead to less accuracy.

To assess the accuracy of both solvers in the presence of flow dynamics such as mixing layers and seperation several things could be recommended. Simulations could be performed, such as for instance a backward facing step to generate mesh guidelines for a seperation bubble. For the temperature several suggestions were given in section 6.1.1. One could also perform a mesh sensitivity study. But this is very expensive taking the fact into account that the mesh currently used cost around 100.000 CPU hours.

6.1.5. What about meshing strategies?

As seen in section 3.3 the general strategy during meshing was to use extruded polyhydral cells whenever possible, and full polyhydral cells otherwise. The prism layer was in general extended from the wall as far as possible, and stretching ratios were kept small (1.05). These last two parameters are interesting to play around with. Both decreasing the prism layer thickness, and increasing the stretching ratio will decrease the number of cells in the mesh. Furthermore, in complex geometries it is in general not possible to use a thick prism layer. It is recommended that this is invesigated further. Results obtained with STAR-CCM+ for this thesis have caught the eye of CD-Adapco. These meshing strategies will be further investigated in cooperation with Prof. M. Peric, currently working for CD-Adapco.

6.2. Conclusions

As seen in section 4 good accuracy can be obtained for simple flows, such as pipe and channel flows, using the standard off-the-shelf finite volume packages: OpenFOAM and STAR-CCM+. Even using the more complex cell types extruded polyhydral cells and full polyhydral cells, it was shown that accurate results can be obtained. But what about the accuracy in a complex geometry such as a T-junction? As was seen in section 5 compromises have to be made for the convection differencing scheme used for the temperature. Combine this with the added flow dynamics in the T-junction (the sharp interface between hot and cold parts of the flow, the seperation zone and mixing layer) and a decreased accuracy can be expected. This can be assesed by a-posteriori calculation of the amount of blending introduced by the vanLeer CDS.

7. Summary

It was seen that performing a DNS in complex geometries is asked for by the problem of thermal fatigue. Performing a DNS in complex geometries calls for the use of methods, the 2nd order accurate FVM, and cell types, extruded polyhydral cells and full polyhydral cells, which are normally not used for a DNS. It was shown that pipe and channel flows can be calculated within a few percent of the references when comparing the RMS of the fluctuations. Moving to complex geometries mesh strategies were described together with compromises in the solver settings. In conclusion it can be said that these methods and cell types can be used with confidence in predicting the channel and pipe flows. If more complex geometries, such as a T-junction, are used, results can still be considered highly accurate. To exactly quantify the accuracy for these geometries more analysis needs to be done.

Bibliography

[1] J.D. Anderson. *Fundamentals of Aerodynamics*. McGraw-Hill, 2006.

[2] G.K. Batchelor. Small-scale variation of convected quantities like temperature in turbulent fluid. *Fluid Mech*, 5:113–133, 1958.

[3] R Bergant. *Turbulent Heat Transfer near the Flat Wall for High Prandtl Numbers*. PhD thesis, University of Ljubljana, Faculty of Mathematics and Physics, 2005.

[4] G. Brethouwer, B.J. Boersma, M.B.J.M. Pourquiè, and F.T.M. Nieuwstadt. Direct numerical simulation of turbulent mixing of a passive scalar in pipe flow. *European Journal of Mechanics - B/Fluids*, 18:739–756, 1999.

[5] W.D. jr. Callister. *Materials Science and Engineering, An Introduction*. John Wiley and Sons, Inc., 2003.

[6] CD-Adapco. Cd-adapco, May 2011. `http://www.cd-adapco.com`.

[7] S. Chapulot, C. Gourding, T. Payen, J.P. Magnaud, and A. Monavon. Hydro-thermal-mechanical analysis of thermal fatigue in a mixing tee. *Nuclear Engineering and Design*, pages 575–596, 2005.

[8] A Chatelain. *Simulation des Grandes Echelles d'écoulements turbulents avec transferts de chaleur*. PhD thesis, INSTITUT NATIONAL POLYTECHNIQUE DE GRENOBLE, September 2004.

[9] P.A. Davidson. *Turbulence*. Oxford University Press, 2004.

[10] E de Villiers. *The Potential of Large Eddy Simulation for the Modeling of Wall Bounded Flows*. PhD thesis, Imperial College of Science, Technology and Medicine, July 2006.

[11] J.G.M. Eggels. *Direct and Large Eddy Simulation of Turbulent Flow in a Cylindrical Pipe Geometry*. PhD thesis, Delft University of Technology, February 1994.

[12] N.F. Felten and T.S. Lund. Kinetic energy conservation issues associated with the collocated mesh scheme for incompressible flow. *Journal of Computational Physics*, 215:465–484, 2006.

[13] J. H. Ferziger and M. Perić. *Computational Methods for fluid dynamics*. Springer, 2002.

[14] J. Fokken, R. Kapulla, G. Galgani, O. Schib, K. Pawa, and H.M. Prasser. Lif-measurements and self-similarity considerations in a stably stratified isokinetic turbulent mixing layer. In *Lasermethoden in der Strmungsmesstechnik*, 2010.

[15] N. Fukushima, K. Fukagata, N. Kasagi, H. Noguchi, and K. Tanimoto. Numerical and experimental study on turbulent thermal mixing in a T-junction flow. In *The 6th ASME-JSME Thermal Engineering Joint Conference*, 2003.

[16] Kawamura H. DNS database of wall turbulence and heat transfer at tokyo university of science, September 2010. `http://murasun.me.noda.tus.ac.jp/turbulence/`.

[17] R.I. Issa. Solution of the implicit discretised fluid flow equations by operator-splitting. *Journal of computational physics*, 62:40–65, 1985.

[18] H Jasak. *Error Analysis and Estimation for the Finite Volume Method with Applications to Fluid Flows*. PhD thesis, Imperial College of Science, Technology and Medicine, June 1996.

[19] S.T. Jayaraju, E.M.J. Komen, and E. Baglietto. Suitability of wall-functions in large eddy simulations for thermal fatigue in a T-junction. *Nuclear Engineering and Design*, 240:2544–2554, 2010.

[20] A.N. Kolmogorov. The local structure of turbulence in incompressible viscous fluid for very large Reynolds numbers. *Proceedings: Mathematical and Physical Sciences*, 434:9–13, 1991.

[21] M. Kozuka, Y. Seki, and H. Kawamura. DNS of turbulent heat transfer in a channel flow with high spatial resolution. *International Journal of Heat and Fluid Flow*, 30:514–524, 2009.

[22] A.K. Kuczaj and E.M.J. Komen. Large-eddy simulation study of turbulent mixing in a T-junction. In *XCFD4NRS, Grenoble*, 2008.

[23] S. Kuhn, O. Braillard, B. Niceno, and H Prasser. Computational study of conjugate heat transfer in t-junctions. *Nuclear Engineering and Design*, 240:1548–1557, 2010.

[24] M. Merzari, A. Khakim, H. Ninokata, and E. Baglietto. Toward an accurate approach for the prediction of the flow in a T-junction: URANS. *Nuclear Engineering and Technology*, 41:1191–1204, 2009.

[25] Y. Na and T.J. Hanratty. Limiting behavior of turbulent scalar transport close to a wall. *Int. Journal of Heat and Mass transfer*, 43:1749–1758, 2000.

[26] OpenCFD. Openfoam, May 2011. `http://www.openfoam.com`.

[27] C. Peniguel, M. Sakiz, S. Benhamadouche, J.M. Stephan, and C. Vindeirinho. Presentation of a numerical 3D approach to tackle thermal striping in a PWR nuclear T-junction. In *ASME PVP*, 2003.

[28] S.B. Pope. *Turbulent flows*. Cambridge University Press, 2000.

[29] L. Redjem-Saad, M. Ould-Rouiss, and G. Lauriat. Direct numerical simulation of turbulent heat transfer in pipe flows: Effect of prandlt number. *International Journal of Heat and Fluid Flow*, 28:847–861, 2007.

[30] M. Schmid, G. Deng, V. Seidl, M. Visonneau, and M. Peric. Computation of complex turbulent flows. *Notes on Numerical Fluid Mechanics*, 66:407–425, 1998.

[31] B.L. Smith. Thermal fatigue in T-junctions: Experimantation and modelling. In *THINS Student Course and Workshops*, 2011.

[32] STAR-CCM+. *User manual, version 6.02.007*. CD Adapco, 2011.

[33] I. Tiselj, R. Bergant, B. Mavko, I. Bajsic, and G. Hetsroni. DNS of turbulent heat transfer in channel flow with heat conduction in the solid wall. *Journal of Heat Transfer*, 123:849–857, 2001.

[34] R.W.C.P. Verstappen and A.E.P. Veldman. Preserving symmetry in convection-diffusion schemes. *Turbulent Flow Computation*, pages 75–100, 2002.

[35] J. Westin. High-cycle thermal fatigue in mixing tees; large-eddy simulations compared to a new validation experiment. In *ICONE16, Orlando*, 2008.

[36] F.M. White. *Viscous Fluid Flow*. McGraw-Hill, 2006.

A. Finite volume discretization in OpenFOAM

This appendix describes the discretization within the finite volume framework of continuous PDE's. The first step is to descritize the solution domain, described in section A.1. The second step is to descritize the continous transport equation, this is discussed in section A.2.

This appendix is essentially a summary of chapter three of the thesis written by Hrvoje Jasak[18].

A.1. Discretization of the solution domain in OpenFOAM

The solution domain is divided in control volumes. An example of such a control volume can be seen in figure A.1. The shape of the control volumes is arbitrary in the sense that the number of faces is not limited. These volumes are generally called polyhedral cells. The following rules apply to the control volumes:

- all faces are flat
- the point P is located at the centroid of the control volume
- all unknowns are defined at the point P (collocated grids)
- the control volumes are constant in time

The fact that the point P is located at the centroid of the control volume yields the following equation:

$$\int_{V_p} (\mathbf{x} - \mathbf{x}_P) dV = \mathbf{0} \tag{A.1.1}$$

The centroid of the faces will also be used during the discretization, the centroid of a face is defined by:

$$\int_{f} (\mathbf{x} - \mathbf{x}_f) d\mathbf{S} = \mathbf{0} \tag{A.1.2}$$

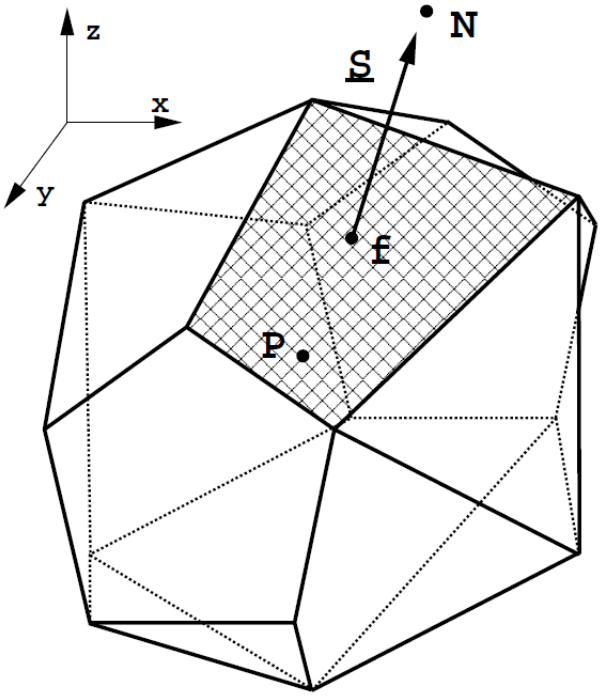

Figure A.1.: A polyhedral control volume. The centroid of the control volume is located at P. The vector **S** is normal to the cell face it belongs to and the size of **S** is equal to the area of the face. N is the cell center of the neighbouring cell. [18]

A.2. Discretization of the transport equation in OpenFOAM

The discretization of the transport equation is presented in this section. The transport equation is a template for all equations solved by OpenFOAM. Please note that this general form of the transport equation is also valid for the momentum equation in OpenFOAM since non-linearity is lagged, see section 3.2.3.

The general form of the transport equation for scalar ϕ is:

$$\frac{\partial \phi}{\partial t} + \nabla \cdot (\mathbf{U}\phi) - \nabla \cdot (\Gamma_\phi \nabla \phi) = S_\phi(\phi) \tag{A.2.1}$$

Where we can see the temporal term, convection term, diffusion term and source term. Please note that the density, which one would expect in this equation, is already neglected since only incompressible flows are considered in this thesis.

In the finite volume framework this yields the following integral for the transport equa-

tion over a control volume around P:

$$\int_t^{t+\delta t}\left[\frac{\partial}{\partial t}\int_{V_P}\phi dV+\int_{V_P}\nabla\cdot(\mathbf{U}\phi)dV-\int_{V_P}\nabla\cdot(\Gamma_\phi\nabla\phi)dV\right]dt = \int_t^{t+\delta t}\left[\int_{V_P}S_\phi(\phi)dV\right]dt \tag{A.2.2}$$

Furthermore it is assumed that the value of ϕ varies linear in space and time, giving:

$$\phi(\mathbf{x})=\phi_P+(\mathbf{x}-\mathbf{x}_P)\cdot(\nabla\phi)_P \tag{A.2.3}$$

$$\phi(t+\Delta t)=\phi^t+\Delta t\left(\frac{\partial\phi}{\partial t}\right)^t \tag{A.2.4}$$

In the transport equation it can be recognized that the convection and diffusion terms contain the divergence operator in the integral and that the temporal and source terms do not. Let us first consider the terms which are not under the divergence operator (thus the temporal and source terms). These volume integrals can be evaluated as follows:

$$\int_{V_p}\phi(\mathbf{x})dV=\int_{V_p}[\phi_P+(\mathbf{x}-\mathbf{x}_P)\cdot(\nabla\phi)_P]dV=\phi_P\int_{V_p}dV+\left[\int_{V_p}(\mathbf{x}-\mathbf{x}_P)dV\right]\cdot(\nabla\phi)_P \tag{A.2.5}$$

Using the fact that P is located at the centroid of the volume (see equation A.1.1) the second term can be eliminated, yielding:

$$\int_{V_p}\phi(\mathbf{x})dV=\phi_P V_P \tag{A.2.6}$$

The volume integrals that contain terms under the divergence operator (the convection and diffusion term) are treated differently. Gauss' theorem is used for this:

$$\int_{V_p}\nabla\cdot\mathbf{a}dV=\int_{\partial V_p}d\mathbf{S}\cdot\mathbf{a} \tag{A.2.7}$$

Using the fact that the control volume has a finite number of faces the face integral can be split in a sum of face integrals over these faces:

$$\int_{\partial V_p} d\mathbf{S} \cdot \mathbf{a} = \sum_f \left(\int_f d\mathbf{S} \cdot \mathbf{a} \right) \tag{A.2.8}$$

The face integral under the summation sign can be rewritten:

$$\int_f d\mathbf{S} \cdot \mathbf{a} = \left(\int_f d\mathbf{S} \right) \cdot \mathbf{a}_f + \left[\int_f d\mathbf{S}(\mathbf{x} - \mathbf{x}_f) \right] : (\nabla \mathbf{a})_f \tag{A.2.9}$$

Now equation A.1.2 can be used to eliminate the second term:

$$\left(\int_f d\mathbf{S} \right) \cdot \mathbf{a}_f + \left[\int_f d\mathbf{S}(\mathbf{x} - \mathbf{x}_f) \right] : (\nabla \mathbf{a})_f = \left(\int_f d\mathbf{S} \right) \cdot \mathbf{a}_f = \mathbf{S} \cdot \mathbf{a}_f \tag{A.2.10}$$

Now the volume integrals with terms under the divergence operator can we written as:

$$\int_{V_P} \nabla \cdot \mathbf{a} dV = \sum_f \mathbf{S} \cdot \mathbf{a}_f \tag{A.2.11}$$

As can be seen the values of $\mathbf{a}$ are needed at the faces of the cells ($\mathbf{a}_f$). This will be discussed in the following sections when the terms in the transport equation are treated term by term.

A.2.1. Convection term

The convection term is a volume integral that contains a term under the divergence operator, therefore it can be discretized using equation A.2.11:

$$\int_{V_P} \nabla \cdot (\mathbf{U}\phi) dV = \sum_f \mathbf{S} \cdot (\mathbf{U}\phi)_f = \sum_f \mathbf{S} \cdot \mathbf{U}_f \phi_f \tag{A.2.12}$$

The face flux is introduced as:

$$F = \mathbf{S} \cdot \mathbf{U}_f \tag{A.2.13}$$

This results in the following discretization for the convection term:

$$\int_{V_P} \nabla \cdot (\mathbf{U}\phi) dV = \sum_f F\phi_f \tag{A.2.14}$$

The values of ϕ_f are interpolated from the cell centers to the cells faces using the convection differencing scheme. The different possibilities (schemes) which can be used for this interpolation are discussed in section A.3

A.2.2. Diffusion term

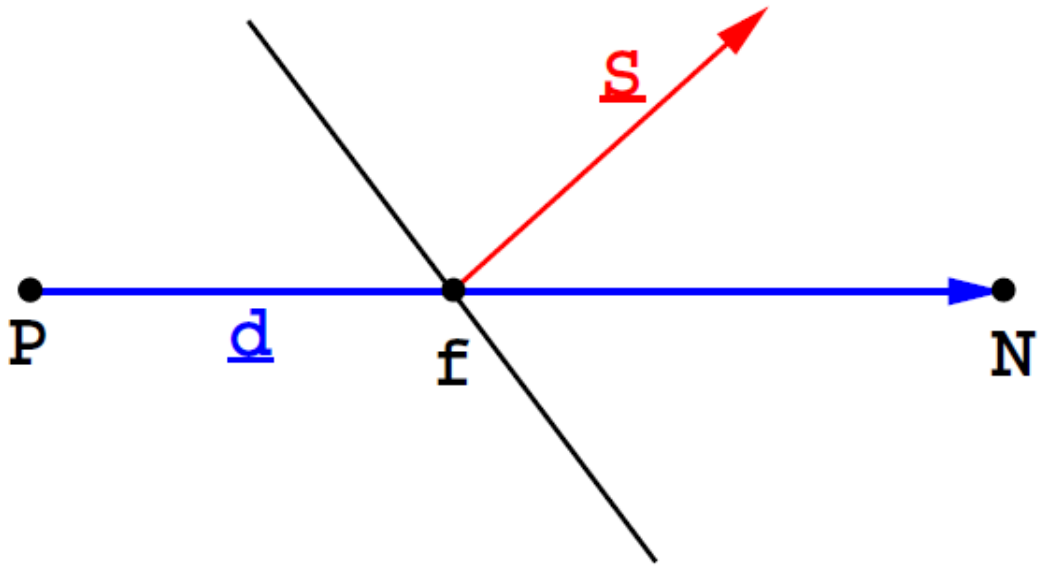

Figure A.2.: A non-orthogonal face [18]

The diffusion term is discretized in a similar manner as the convective term:

$$\int_{V_P} \nabla \cdot (\Gamma_\phi \nabla\phi) dV = \sum_f \mathbf{S} \cdot (\Gamma_\phi \nabla\phi)_f = \sum_f (\Gamma_\phi)_f \mathbf{S} \cdot (\nabla\phi)_f \tag{A.2.15}$$

The interpolation of the diffusion constant Γ_ϕ is performed using one of the convection differencing schemes as described in section A.3. For determining the gradient of ϕ ($\nabla\phi$) a straightforward discretization would be:

$$\mathbf{S} \cdot (\nabla\phi)_f = |\mathbf{S}| \frac{\phi_N - \phi_P}{|\mathbf{d}|} \tag{A.2.16}$$

However, this discretization is only possible when **d** and **S** are parallel. This is known as an orthogonal face. An example of a non-orthogonal face can be seen in figure A.2. For the treatment of the non-orthogonal faces the following procedure is used:

The correction for non-orthogonal faces is performed in OpenFOAM using a combination of the orthogonal correction approach and the over-relaxed approach. It consists of splitting the face vector into an ortogonal and non-orthogonal part:

$$\mathbf{S} = \Delta + k \tag{A.2.17}$$

The following combination is made:

$$\Delta = \frac{d|\mathbf{S}|}{\Delta_{coeff}} \tag{A.2.18}$$

where:

$$\Delta_{coeff} = max(\frac{d\mathbf{S}}{|\mathbf{S}|}, 0.05|d|) \tag{A.2.19}$$

The discretization of the dissipation term then becomes:

$$\mathbf{S}(\nabla\phi)_f = \Delta(\nabla\phi)_f + k(\nabla\phi)_f \tag{A.2.20}$$

Using the following discretizations:

$$\Delta(\nabla\phi)_f = |\mathbf{S}|\frac{\phi_N - \phi_P}{|d|} \tag{A.2.21}$$

$$k(\nabla\phi)_f = k(f_x(\nabla\phi)_P + (1 - f_x)(\nabla\phi)_N) \tag{A.2.22}$$

where:

$$(\nabla\phi)_P = \frac{1}{V_P}\sum_f \mathbf{S}\phi_f \tag{A.2.23}$$

A.2.3. Source term

Before the source term is discretized it is linearized as follows:

$$S_\phi(\phi) = Su + Sp\phi \tag{A.2.24}$$

This gives the following discretization (using equation A.2.6):

$$\int_{V_P} S_\phi(\phi) dV = SuV_P + SpV_P\phi \tag{A.2.25}$$

A.2.4. Temporal term

The volume integral containing the temporal derivative can be discretized using equation A.2.6. Futhermore the fact that the control volumes are constant in time is used to interchange the integral operator and derivation operator:

$$\frac{\partial}{\partial t}\int_{V_P} \phi dV = \int_{V_P} \frac{\partial \phi}{\partial t} dV = \frac{\partial \phi}{\partial t} V_P \tag{A.2.26}$$

All the terms in equation A.2.2 are now discretized in space. The integrals in time in equation A.2.2 are simply neglected. This means that variations in time of the convection, diffussion and source terms are neglected and that the temporal derivative is assumed to be constant.

Using these assumptions and the discretizations for for the convective, diffusive and source terms equation A.2.2 can be written as:

$$\frac{\partial \phi}{\partial t}_P V_P + \sum_f F\phi_f - \sum_f (\Gamma_\phi)_f \mathbf{S} \cdot (\nabla\phi)_f = SuV_P + SpV_P\phi \tag{A.2.27}$$

The temporal derivative is discretized using backward differencing. First create two Taylor series expansions:

$$\phi^{n-1} = \phi^n - \frac{\partial \phi}{\partial t}\Delta t + \frac{1}{2}\frac{\partial^2 \phi}{\partial t^2}\Delta t^2 + O(\Delta t^3) \tag{A.2.28}$$

$$\phi^{n-2} = \phi^n - 2\frac{\partial \phi}{\partial t}\Delta t + 2\frac{\partial^2 \phi}{\partial t^2}\Delta t^2 + O(\Delta t^3) \tag{A.2.29}$$

Now the discretization of the temporal derivative can be constructed:

$$\frac{\partial \phi}{\partial t} = \frac{\frac{3}{2}\phi^n - 2\phi^{n-1} + \frac{1}{2}\phi^{n-2}}{\Delta t} \tag{A.2.30}$$

A.2.5. Final form of the discretized transport equation

Putting all the discretized terms together the final form of the transport equation now becomes:

$$\frac{\frac{3}{2}\phi^n - 2\phi^{n-1} + \frac{1}{2}\phi^{n-2}}{\Delta t} V_P + \sum_f F\phi_f - \sum_f (\Gamma_\phi)_f \mathbf{S} \cdot (\nabla\phi)_f = SuV_P + SpV_P\phi \tag{A.2.31}$$

A.3. Convection differencing scheme

For the discretization of the convection term the values of the velocities need to be interpolated to the cell faces. This is the famous convection differencing scheme, see Figure A.3.

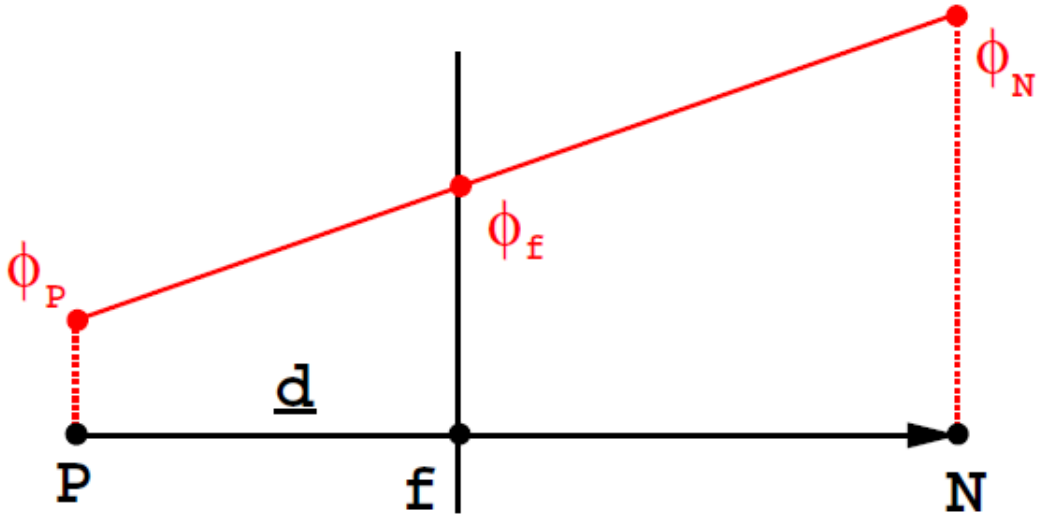

Figure A.3.: Face interpolation. For calculation of the face fluxes (A.2.13) the values at the cell centers (P and N) need to be interpolated to the cells face using the convection differencing scheme.) [18]

For the face interpolation various schemes exist. It seems straightforward to just interpolate the values from the cell-centers to the cell-faces using linear interpolation. However, this will often lead to numerical instabilities. To overcome this problem of instability numerous schemes exist. The list given in this appendix does certainly not

cover all of the schemes available in literature but simply lists the schemes used in this thesis.

A.3.1. Linear convection differencing scheme

Using linear discretization the face value is calculated as follows:

$$\phi_f = f_x \phi_P + (1 - f_x)\phi_N \tag{A.3.1}$$

where (see Figure A.3):

$$f_x = \frac{\overline{fN}}{\overline{PN}} \tag{A.3.2}$$

A.3.2. Upwind convection differencing scheme

The upwind scheme does not interpolate the values but simply picks the value of the cell center which is upwind of the face. The cell center which is upwind of the face is determined using the face flux as follows:

$$\phi_f = \phi_P \quad for \quad F \geq 0 \tag{A.3.3}$$

$$\phi_f = \phi_N \quad for \quad F < 0 \tag{A.3.4}$$

A.3.3. LinearUpwind convection differencing scheme

The linear upwind scheme is also known as the second order upwind scheme. It applies a correction to the upwind scheme as follows:

$$\phi_f = \phi_P + (\mathbf{x}_f - \mathbf{x}_P) \cdot (\nabla\phi)_P \quad for \quad F \geq 0 \tag{A.3.5}$$

$$\phi_f = \phi_N + (\mathbf{x}_f - \mathbf{x}_N) \cdot (\nabla\phi)_N \quad for \quad F < 0 \tag{A.3.6}$$

The gradient at the cell centers is calculated using equation A.2.23.

A.3.4. Blended convection differencing scheme

blended, using blending factor γ

$$\phi_f = (1-\gamma)(\phi_f)_{UD} + \gamma(\phi_f)_{CD} \tag{A.3.7}$$

A.3.5. MidPoint convection differencing scheme

$$\phi_f = \frac{1}{2}\phi_P + \frac{1}{2}\phi_N \tag{A.3.8}$$

A.3.6. ClippedLinear convection differencing scheme

clippedLinear, using clipping factor γ:

$$\phi_f = f_{x,clipped}\phi_P + (1 - f_{x,clipped})\phi_N \tag{A.3.9}$$

where:

$$f_{x,clipped} = max(min(f_x, 1 - \frac{\gamma}{1+\gamma}), \frac{\gamma}{1+\gamma}) \tag{A.3.10}$$

In this scheme the value of f_x is set to a maximum (or minumum), determined by the clipping factor. This effectively reduces the instabilities originating from the stretched part of the mesh.

A.3.7. VanLeer convection differencing scheme

The vanLeer scheme applies blending between linear and upwind locally in the domain based on a smoothness criterion (see Figure A.4):

$$r = \frac{\phi_C - \phi_U}{\phi_D - \phi_C} \tag{A.3.11}$$

This criterion is essentialy the ratio of consecutive gradients. Using this smoothness criterion a limiter function is calculated:

$$\Psi = \frac{r + |r|}{1 + |r|} \tag{A.3.12}$$

Using this limiter the following combination between upwind (UD) and linear (CD) is made:

$$\phi_f = (\phi_f)_{UD} + \Psi((\phi_f)_{CD} - (\phi_f)_{UD}) \tag{A.3.13}$$

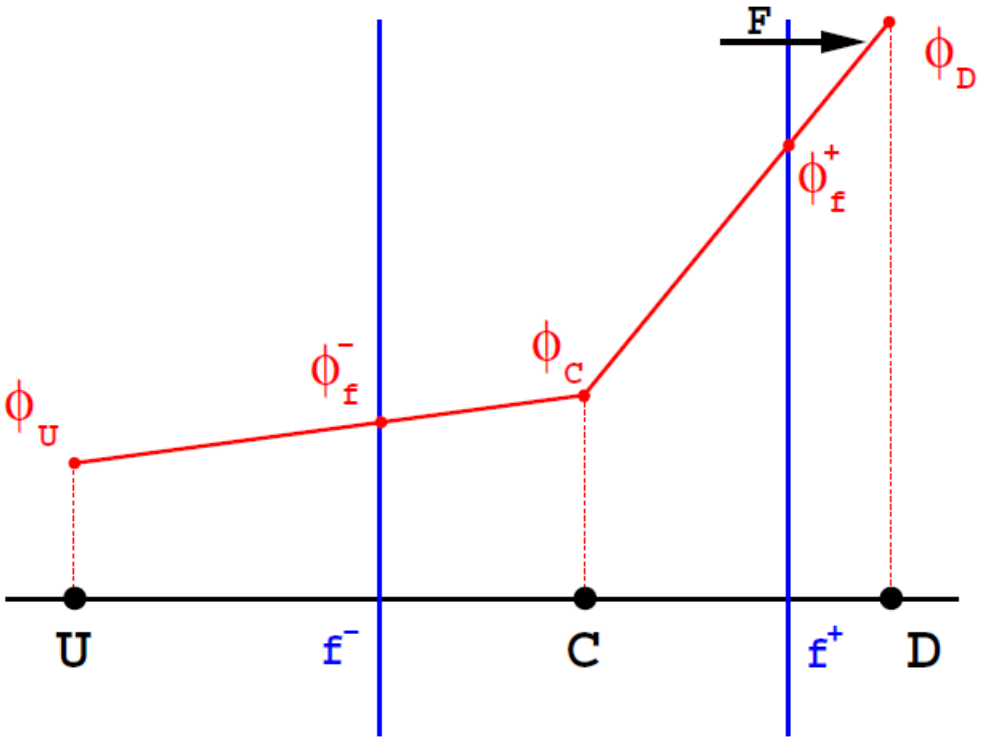

Figure A.4.: The smoothness criterion. Based on the face flux F the far upwind cell U is determined. Next the smoothness criterion can be calculated using equation A.3.11. [18]

A.3.8. Bounded central convection differencing scheme

The bounded central scheme is implemented in STAR-CCM+ and not in OpenFOAM. It uses the normalized variable approach. The normalized variable is defined as [18]:

$$\tilde{\phi}_C = \frac{\phi_C - \phi_U}{\phi_D - \phi_U} \tag{A.3.14}$$

The scheme is than constructed as a combination of upwind (UD), linear (CD) and the linearUpwind (LUD) CDS. Upwind factor γ is used [32]:

$$\phi_f = \phi_{UD} \quad for \quad \tilde{\phi}_C < 0 \quad or \quad \tilde{\phi}_C > 1 \tag{A.3.15}$$

$$\phi_f = \sigma(\tilde{\phi}_C)\phi_{CD} + (1 - \sigma(\tilde{\phi}_C))\phi_{LUD} \quad for \quad 0 \geq \tilde{\phi}_C \leq 1 \tag{A.3.16}$$

where $\sigma(\tilde{\phi}_C)$ is a function of the normalized variable. The following rules apply to $\sigma(\tilde{\phi}_C)$:

$$\sigma(0) = 0 \quad and \quad \sigma(\tilde{\phi}_C) = 1 \quad for \quad \gamma \leq \tilde{\phi}_C \tag{A.3.17}$$

The variation of $\sigma(\tilde{\phi}_C)$ for $0 < \tilde{\phi}_C < \gamma$ is not provided by the user manual of STAR-CCM+ [32].

B. Kinetic energy conservation properties of convection differencing schemes

This section briefly shows how the conservation of kinetic energy of a certain scheme can be analyzed. As recognized by [12] this is of vital importance for stability and accuracy of a simulation using unstructered meshes. It is well known that the upwind scheme is diffusive and acts as a sink for kinetic energy. In this section it is shown that the linear convection differencing scheme can produce a kinetic energy sink leading to numerical diffusion, but is can also act as a source leading to instability of the simulation. The procedure used in this section is inspired by [34].

Starting from the momentum equation, neglecting any sources and the diffusion term:

$$\int_t^{t+\delta t} \left[\frac{\partial}{\partial t} \int_{V_P} \mathbf{U} dV + \int_{V_P} \nabla \cdot (\mathbf{U}\mathbf{U}) dV \right] = 0 \tag{B.0.1}$$

Transform this into the semi-discrete form (see section A.2):

$$V_P \frac{d\mathbf{U}}{dt} = -\sum_f F\mathbf{U}_f \tag{B.0.2}$$

This can be rewritten:

$$V_P \frac{d\mathbf{U}}{dt} = -\sum_f F\mathbf{U}_f = -\mathbf{C}(F)\mathbf{U} \tag{B.0.3}$$

In this equation the matrix $\mathbf{C}(F)$ contains both the face fluxes and the convection differencing scheme.

Since the velocity at the face is not known on our collocated grid the velocities need to be interpolated from the cell centers to the cell faces. For this interpolation one needs to choose a scheme. Numerous options are available such as upwind, linear and midPoint (see Appendix A.3). The choice of this scheme will determine the shape of the matrix $\mathbf{C}(F)$.

From equation B.0.2 the evolution of the kinetic energy ($\| \mathbf{U} \|^2 = \mathbf{U}^T\mathbf{V}\mathbf{U}$, $\mathbf{V}$ is the diagonal matrix containing the cell volumes) in time can be written as:

$$\frac{d}{dt} \| \mathbf{U} \|^2 = -\mathbf{U}^T(\mathbf{C}(F) + \mathbf{C}(F)^T)\mathbf{U} \tag{B.0.4}$$

It can be seen here that the matrix needs to be skew-symmetric to make the right hand side equal to zero for arbitrary $\mathbf{U}$. If the right hand side is zero the convection differencing scheme will conserve kinetic energy.

It is not difficult to prove that the matrix $\mathbf{C}(F)$ will be skew-symmetric if midPoint interpolation is used:

$$\mathbf{U}_f = \frac{1}{2}\mathbf{U}_P + \frac{1}{2}\mathbf{U}_N \tag{B.0.5}$$

Now write this matrix for a simple tet cell such as in figure B.1. The matrix $\mathbf{C}(F)$ will be:

$$\mathbf{C}(F) = \begin{bmatrix} \frac{1}{2}\sum_f F & 0 & 0 & -\frac{1}{2}F_1 \\ 0 & \frac{1}{2}\sum_f F & 0 & -\frac{1}{2}F_2 \\ 0 & 0 & \frac{1}{2}\sum_f F & -\frac{1}{2}F_3 \\ \frac{1}{2}F_1 & \frac{1}{2}F_2 & \frac{1}{2}F_3 & \frac{1}{2}\sum_f F \end{bmatrix} \tag{B.0.6}$$

Which is a sub-matrix of the entire $\mathbf{C}(F)$ matrix for an arbitrary mesh. The number of faces of a cell will simply determine the size of the sub-matrix. $\frac{1}{2}\sum_f F$ is the sum of all face fluxes for a cell. In theory this should be zero, in practice this will have a small value.

The drawbacks of using the midPoint interpolation are:

- decrease in order of accuracy
- phase error

However, these drawbacks dissappear in parts of the mesh where there is no cell-stretching.

Using this analysis it can be concluded that the midPoint scheme is kinetic energy conservative. Using the upwind scheme will always decrease kinetic energy, using the downwind scheme will always increase kinetic energy. Using the linear scheme on stretched meshes could give either decrease or increase. An increase can lead to instabilities.

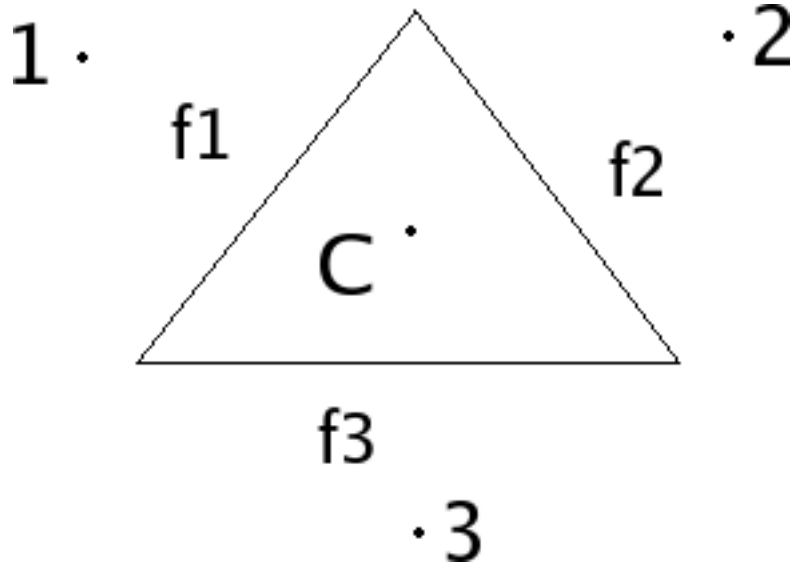

Figure B.1.: A 2D tet cell with its neighbours. The cell center is indicated by C. The neighbour cell centers are indicated by 1,2 and 3. The three different faces are indicated by f1,f2 and f3.